



Large-Eddy Simulations of Spray a Flames Using Explicit Coupling of the Energy Equation with the FGM Database

Constantin Sula¹ · Holger Grosshans² · Miltiadis V. Papalexandris¹

Received: 17 September 2021 / Accepted: 1 February 2022 / Published online: 25 February 2022
© The Author(s), under exclusive licence to Springer Nature B.V. 2022

Abstract

This paper provides a numerical study on n-dodecane flames using Large-Eddy Simulations (LES) along with the Flamelet Generated Manifold (FGM) method for combustion modeling. The computational setup follows the Engine Combustion Network Spray A operating condition, which consists of a single-hole spray injection into a constant volume vessel. Herein we propose a novel approach for the coupling of the energy equation with the FGM database for spray combustion simulations. Namely, the energy equation is solved in terms of the sensible enthalpy, while the heat of combustion is calculated from the FGM database. This approach decreases the computational cost of the simulation because it does not require a precise computation of the entire composition of the mixture. The flamelet database is generated by simulating a series of counterflow diffusion flames with two popular chemical kinetics mechanisms for n-dodecane. Further, the secondary breakup of the droplet is taken into account by a recently developed modified version of the Taylor Analogy Breakup model. The numerical results show that the proposed methodology captures accurately the main characteristics of the reacting spray, such as mixture formation, ignition delay time, and flame lift-off. Additionally, it captures the “cool flame” between the flame lift-off and the injection nozzle. Overall, the simulations show differences between the two kinetics mechanisms regarding the ignition characteristics, while similar flame structures are observed once the flame is stabilised at the lift-off distance.

Keywords Spray combustion · Combustion modeling · Large-eddy simulations · Flamelet generated manifolds · N-docecane

✉ Miltiadis V. Papalexandris
miltos@uclouvain.be

Constantin Sula
constantin.sula@uclouvain.be

Holger Grosshans
holger.grosshans@ptb.de

¹ Institute of Mechanics, Materials and Civil Engineering, Université catholique de Louvain, Place du Levant 2, 1348 Louvain-la-Neuve, Belgium

² Physikalisch-Technische Bundesanstalt (PTB), Bundesallee 100, 38116 Braunschweig, Germany

1 Introduction

Spray combustion is encountered in many industrial applications, one significant class being Diesel engines. Over the last decades, numerous investigations have been carried out with the aim of improving their efficiency and reducing pollutants. Owing to the ever-increasing computing power, many such investigations on engine improvement nowadays involve numerical simulations. The main advantages of numerical simulations compared to experiments are their cost-efficiency and the easy access to flow quantities governed by small time scales. For example, mixture composition and size distribution of soot particles are experimentally difficult or sometimes even impossible to obtain.

Diesel combustion is primarily mixing controlled because the liquid fuel is usually injected into the chamber as a high-velocity jet through a nozzle. For such configurations, combustion of the fuel-air mixture involves a series of complex phenomena, including atomization, breakup and dispersion of the droplets, along with the impact on the turbulence and the strongly coupled evaporation and combustion process. All these physical and chemical processes are developing in a large range of spatial and temporal scales. The resolution of all these scales on a numerical mesh leads to an unaffordable computational cost. Consequently, different assumptions have to be introduced in order to derive simplified models. However, these assumptions entail new uncertainties that require careful validation.

To address these issues, the Engine Combustion Network (ECN) (2021) has defined a simplified study case known as *Spray A*, which is a single-nozzle spray with boundary conditions that closely match the characteristics of Diesel-like combustion chambers. N-dodecane was identified as a suitable surrogate for Diesel fuel due to the long carbon chain and the well defined thermophysical properties Cernansky et al. (2007). Additionally, the ECN provides experimental measurements of global quantities, e.g., Ignition Delay Time (IDT) and Flame Lift-Off Length (FLOL), for a range of ambient and injections conditions.

Regarding spray modeling, the existing literature is quite extensive, and many numerical studies can be found therein. Typically, the fuel spray poses a very short liquid core due to rapid atomization and evaporation in engine conditions. For this reason, a widely used approach is to model the atomization process by applying a specific initial droplet size distribution, whereas the secondary droplet breakup is taken into account by a sub-model. Various models with different levels of accuracy and complexity have been developed and successfully applied to spray flows Sirignano (2010). Studies of non-reactive sprays Grosshans et al. (2015); Nicholson et al. (2018); Sula et al. (2020), showed that the Lagrangian Particle Tracking method in conjunction with the Large Eddy Simulation (LES) approach can accurately capture the main characteristics of the spray jet, e.g., liquid length, vapour penetration distance and mixture formation.

Performing a fuel spray simulation requires a combustion model with the capacity to accommodate complex chemical kinetic while taking into account Turbulence-Chemistry Interactions (TCI) in a reliable manner. To this end, different turbulent combustion models have been coupled with the LES approach, including the perfectly stirred reactor Fooladgar et al. (2017), the conditional moment closure Blombert et al. (2016), the sparse Lagrangian multiple mapping conditioning Salehi et al. (2017), to mention but a few. However, the application of these models is still computationally demanding. Additionally, the computational cost increases with the size of the chemical kinetics mechanism. An alternative choice is to employ flamelet-based methods such as Flamelet Generated Manifolds (FGM)

Peters (1984); Van Oijen and De Goey (2000), unsteady flamelet progress variables Pierce and Moin (2004), representative interactive flamelet Barths et al. (2000) and others.

The underlying idea of flamelet-based methods is that the local flame structure is similar to that in a laminar flow but is influenced by the flow field, *e.g.* via strain. In particular, it is assumed that it is considerably thinner compared to the other scales and distortions of the flow. In turn, regarding non-premixed flames, this implies that the chemical reactions are faster than all other flow phenomena and can be assumed to occur within relatively thin layers Peters (1988). Therefore, the internal structure of the flame is approximately “frozen” while it is advected by the flow. Consequently, pre-generated solutions of chemical composition for flames in simple configurations can be used to predict local chemical composition in more complex flows via solution-mapping procedures and functions. In this manner, the computational cost is reduced by essentially decoupling the chemistry and the TCI calculations from the flow solver while using complex chemical kinetics schemes. The TCI in the flamelet based models is accounted for by means of presumed probability functions Peters (1984). To this end, all quantities are stored in a database as a function of a limited number of control variables.

While the most common approach is to construct the FGM tables using three control variables, studies based on Reynolds-Averaged Navier-Stokes simulations Knudsen et al. (2010); Zhang et al. (2019) reported promising results in constructing these tables with four or even more control variables. However, it is important to note that the increase in the number of control variables for the FGM tables significantly impacts the computational cost Zhang et al. (2020). Therefore, in the current study, we construct the FGM database using three control variables, namely, the mean values of the mixture fraction and the progress variable, and the variance of the mixture fraction.

Another challenge when applying the FGM method is the coupling of the algorithms for the computation of the temperature and the mixture properties with the FGM database. Various approaches have appeared in the literature to address this issue. In summary, these methods can be categorized into two principal approaches. The first one is to extend the FGM database with an additional quantity, which is the heat loss compared to the adiabatic reference condition Ma and Roekaerts (2016a, 2016b); Jurić et al. (2021). This approach allows to account for enthalpy losses due to heat transfer between the two phases and for the latent heat of evaporation. This is possible in the application of interest because the temperature of the oxidizer is sufficiently high to allow counterflow diffusion flamelets to exist even in the presence heat loss. According to this methodology, the temperature of the gaseous phase is also recovered from the FGM database.

The second approach is to compute the temperature by solving the energy equation while the transport and thermophysical properties of the mixture are recovered from the FGM database Wehrfritz et al. (2016); Kahila et al. (2018); Tekgül et al. (2020). For instance, Wehrfritz et al. (2016) cast the energy equation in terms of the absolute enthalpy. Additionally, they proposed an optimization procedure to identify a subset of species to approximate the physical properties of the mixture. It is worth mentioning that this optimization procedure is run on every point in the FGM database, and that the set of species are mechanism dependent. Furthermore, this approach is computationally demanding as more quantities must be included in the FGM database, *e.g.* species mass fractions.

The present study is concerned with numerical simulations of turbulent spray combustion under the Spray A operating condition. To this end, a series of LES is carried out using Lagrangian particle tracking to model the dispersed liquid phase and the FGM combustion model to account for the complex chemical reactions. Herein we propose a computationally efficient approach to couple the energy equation with the FGM database

for spray combustion simulations. More specifically, the energy equation is formulated in terms of the sensible enthalpy. The source term due to combustion is then obtained from the FGM database. In this manner, the heat release embodies the effect from all species of the combustion mechanism. Once the sensible enthalpy is computed by integrating the energy equation, then the temperature is computed via the caloric equation of state. The advantage of this approach is that it does not require precise knowledge of the entire composition of the mixture, thereby reducing the workload and memory requirements of the numerical simulation. Moreover, the thermophysical and transport properties of the mixture are computed on the basis of a small number of dominant species recovered from the FGM database through the control variables.

Regarding the secondary breakup of the fuel droplets, the Modified Taylor Analogy Breakup model (MTAB) proposed by Sula et al. (2020) is employed herein. The original TAB model is based upon the analogy between the distortions of a droplet moving through a gas and a second-order harmonic oscillator. In the original model the coefficient that incorporates the effect of the external forces is determined empirically, whereas in MTAB it is computed dynamically as a function of the drag coefficient of the droplet. According to the comparative study of non-reactive Spray A simulations Sula et al. (2020), the MTAB model yields mildly improved estimates for the liquid and vapor penetration lengths than those of the original TAB and the popular Reitz-Diwakar and Pilch-Erdman models. The simulations presented herein are performed using the open-source CFD code OpenFOAM[®] Weller et al. (1998), into which the proposed FGM and MTAB models have been implemented.

Also, a detailed analysis of the flame structure is presented herein, and the numerical results are compared against available experimental data Lillo et al. (2012); Maes et al. (2016); Skeen et al. (2015) and earlier numerical results Wehrfritz et al. (2016); Tekgül et al. (2020). Namely, we investigate how the ignition occurs by quantifying the IDT and the FLOL numerically. Also, we study the concentrations of formaldehyde, hydroxyl and hydrogen peroxide during the combustion process, both in space and time. These species play an important role in the onset of the combustion and the transition from low to high-temperature burning. Additionally, studies have shown that hydrogen peroxide is a good combustion enhancer, and it has a great potential in improving combustion efficiency Nguyen et al. (2014). We assess the ability of the proposed LES-FGM approach to predict the spatial formation of formaldehyde and hydroxide species by comparing the numerical results against the experimental data of Skeen et al. (2015); Maes et al. (2016).

The paper is organized as follows. First, a description of the computational theory and model formulation is provided in Sect. 2, followed by the computational setup and initial conditions in Sect. 3. In Sect. 4, qualitative and quantitative data and analysis of the numerical results are carried out. Finally, Sect. 5 summarizes the findings and concludes the paper.

2 Mathematical and Numerical Modeling

2.1 Governing Equations

The LES of our study are based on the spatially-filtered, compressible Navier-Stokes-Fourier equations. Additionally, the density-weighted operator of Favre (1983) is employed. Applied to a generic quantity ψ , the corresponding Favre-filtered quantity

$\tilde{\psi}$ is defined as $\tilde{\psi} = \overline{\rho\psi}/\bar{\rho}$, where $\bar{\rho}$ and $\overline{\rho\psi}$ are spatially-filtered quantities. To simplify the notation, the quantities associated with the ambient gas will appear without subscript; for example, the gas density will be denoted by ρ . On the other hand, quantities associated with droplets will have a descriptive subscript; *i.e.* the droplet density will be denoted by ρ_d .

Upon spatial filtering, the governing equations describing the balance of mass, momentum and energy of the continuous phase (the surrounding gas) read, Wehrfritz et al. (2016); Sula et al. (2020),

$$\frac{\partial \bar{\rho}}{\partial t} + \nabla \cdot (\bar{\rho} \tilde{\mathbf{u}}) = \bar{\Gamma}, \tag{1}$$

$$\frac{\partial (\bar{\rho} \tilde{\mathbf{u}})}{\partial t} + \nabla \cdot (\bar{\rho} \tilde{\mathbf{u}} \tilde{\mathbf{u}}) = -\nabla \bar{p} + \nabla \cdot \left((\bar{\mu} + \mu_t) \tilde{\mathbf{V}}^d \right) + \bar{\mathbf{F}}, \tag{2}$$

$$\begin{aligned} \frac{\partial (\bar{\rho} \tilde{h}_t)}{\partial t} + \nabla \cdot (\bar{\rho} \tilde{h}_t \tilde{\mathbf{u}}) &= \frac{\partial \bar{p}}{\partial t} + \nabla \cdot \left((\bar{\mu} + \mu_t) \tilde{\mathbf{V}}^d \cdot \tilde{\mathbf{u}} \right) \\ &+ \nabla \cdot \left(\left(\frac{\bar{\kappa}}{\bar{c}_p} + \frac{\kappa_t}{c_p} \right) \nabla \tilde{h}_s \right) + \bar{S}_h + \bar{Q}, \end{aligned} \tag{3}$$

where \bar{p} and $\tilde{\mathbf{u}} = (\tilde{u}, \tilde{v}, \tilde{w})$ denote, respectively, the filtered fluid pressure, and velocity vector. Also, \tilde{h}_t denotes the total “non-chemical” enthalpy, which is the sum of the sensible enthalpy and kinetic energy, *i.e.* $\tilde{h}_t = \tilde{h}_s + \frac{|\tilde{\mathbf{u}}|^2}{2}$. In the above equation $\tilde{\mathbf{V}}^d$ stands for twice the deviatoric part of the filtered strain-rate tensor $\tilde{\mathbf{V}} = \frac{1}{2} (\nabla \tilde{\mathbf{u}} + (\nabla \tilde{\mathbf{u}})^T)$; in other words, $\tilde{\mathbf{V}}^d = 2\tilde{\mathbf{V}} - \frac{2}{3} \nabla \cdot (\bar{\rho} \tilde{\mathbf{u}}) \mathbf{I}$. Additionally, the variables, $\bar{\mu}$, $\bar{\kappa}$, and \bar{c}_p represent the filtered dynamic viscosity, thermal conductivity and heat capacity of the carrier gas.

In the governing system (1, 2, 3) the source terms $\bar{\Gamma}$, $\bar{\mathbf{F}}$ and \bar{Q} describe, respectively, the mass, momentum and energy exchanges between the continuous gaseous phase and the liquid droplets. It is noted that the source term in the energy equation is the sum of two contributions, \bar{S}_h and \bar{Q} respectively. The first term incorporates the energy required to heat the liquid droplets and the latent heat of evaporation of the fuel, while the second term accounts for the heat-release rate due to combustion. The explicit form of the source terms $\bar{\Gamma}$, $\bar{\mathbf{F}}$ and \bar{Q} is provided in Sula et al. (2020) and is not included herein for purposes of economy of space. With regard to \bar{S}_h , it is noted that it is equal to the sum, over all species, of the products between the enthalpies of formation and the reaction rates of the species; see *e.g.* Poinso and Veynante (2005); Papalexandris (2020). Tabulated values of this quantity are provided in the FGM database, the construction of which is discussed in Sect. 2.2 below.

The above balance laws are supplemented with the evolution Eqs. (19) and (20) for the filtered mixture fraction \tilde{Z} and progress variable $\tilde{\mathcal{Y}}$, respectively, and with the algebraic expression (21) for the mixture-fraction variance; these equations are also provided in Sect. 2.2 below. The resulting governing system is closed with the ideal gas law.

Also, as elaborated below, the filtered viscosity and thermal diffusivity of the mixture are computed according to the relations of Wilke (1950) and on the basis of the five dominant species of the reactive gas. For a given species, the kinetic theory of gases, the intermolecular

potential model of a rigid sphere and 7th-order polynomial fits are used to evaluate its transport and thermophysical properties Burcat and Ruscic (2005).

With regard to the subgrid-scale (SGS) modeling, the eddy viscosity μ_t is computed via the dynamic k -equation model Yoshizawa (1987); Chai and Mahesh (2012), while the thermal diffusivity κ_t is computed from μ_t by assuming a constant turbulent Prandtl number, namely, $Pr_t = \frac{c_p \mu_t}{\kappa_t} = 1$. The approach to compute the eddy viscosity is similar to that of the dynamic model Moin et al. (1991) for variable-density flows. However, in this case, the reference velocity is taken to be the square root of the SGS kinetic energy \sqrt{k} instead of $\Delta|\bar{\mathbf{V}}|$, with Δ being the nominal filter width.

The governing Eqs. (1, 2, 3) are then discretized via a finite-volume algorithm and integrated in time via the implicit Euler scheme. With regard to spatial discretization, we employ the second-order upwind scheme for the convective terms and second-order central differences for the diffusive terms. The algorithm for the pressure-velocity coupling is based on the Pressure-Implicit with Splitting of Operators (PISO) technique. This technique was initially introduced in Issa (1986) and herein we employ its generalization to compressible flows Ferziger et al. (2020). We remark that, in our study, we do not invoke the low-Mach number approximation of reacting flows Lessani and Papalexandris (2006), but instead solve numerically the full system (1, 2, 3) for compressible flows. Furthermore, in the computations involving the equation of state, we use the local value of the pressure and not a “background pressure”.

As far as spray modeling is concerned, the Lagrangian particle tracking approach, combined with stochastic parcel method Dukowicz (1980) is employed for the discrete liquid phase. According to this procedure, the droplets are grouped into parcels which are then tracked individually as Lagrangian points. It is also assumed that all droplets in a given parcel share the same properties, namely diameter d , velocity \mathbf{u}_d , density ρ_d , temperature T_d , etc.

Regarding droplet dynamics, we assume that the aerodynamic drag is the only force acting on the liquid-fuel droplets. Thus, their equation of motion reads,

$$\rho_d \frac{d\mathbf{u}_d}{dt} = -\frac{3}{4} \frac{\rho}{d_d} C_D |\mathbf{u}_{rel}| \mathbf{u}_{rel}, \quad (4)$$

where ρ_d is the droplet density, d_d the particle diameter, and \mathbf{u}_{rel} the relative velocity of the droplet with respect to the surrounding gas. Also, C_D stands for the drag coefficient and is dynamically computed via a correlation of the standard drag curve on a smooth sphere Liu et al. (1993). The contribution of the other forces acting on the droplets, such as the virtual mass, Faxen, Basset, Magnus and Saffman forces, are considered negligibly small. This is a common practice in simulation of sprays Grosshans et al. (2015). It is further noted that the term for interphasial drag in Eq. (4) involves the resolved fluid velocities only. This implies that the influence of the subgrid-scale velocity fluctuations in the interphasial drag is ignored.

Finally, it is worth adding that, for any given computational cell, the momentum-exchange term $\bar{\mathbf{F}}$ in the momentum Eq. (2) is the sum of the right-hand side of (4) over all droplets that lie in the cell, divided by the volume of the cell.

The energy balance for a single droplet, neglecting the radiation and the kinetic energy of the evaporated mass, is given by

$$m_d c_{p,d} \frac{dT_d}{dt} = Q_d + \dot{m}_d h_1. \quad (5)$$

Herein T_d is the droplet temperature, $c_{p,d}$ is the specific heat of the liquid, Q_d represents the convective and conductive heat transfer between droplet and surrounding gas, h_l the latent heat of evaporation of the fuel. Also m_d and \dot{m}_d are, respectively, the mass and evaporation rate of a droplet.

In our study, Q_d is approximated by,

$$Q_d = \kappa_d \pi d_d (T - T_d) Nu, \quad (6)$$

with κ_d being the thermal conductivity of the droplet and Nu the Nusselt number. The latter is estimated via Ranz and Marshall (1952a, 1952b),

$$Nu = 2 + 0.6 \sqrt{Re_d} \sqrt[3]{Pr}, \quad (7)$$

where Pr is the Prandtl number with respect to the liquid and Re_d is the Reynolds number of the droplet.

Liquid droplet evaporation is computed via the model proposed in Amsden et al. (1989) which assumes that the fuel droplets are spherical and have uniform properties in their interior. This assumption is justified if the droplet Biot number is less than unity Grosshans et al. (2016), which is the case in the present study. Accordingly, the evaporation rate of a droplet \dot{m}_d is written as,

$$\dot{m}_d = \frac{1}{2} \pi \rho_d d_d^2 \frac{dd_d}{dt}. \quad (8)$$

In the above equation, the rate of decrease of the droplet diameter, on the right-hand side of is approximated via the solution of the Stefan problem in spherical coordinates; the resulting correlation is provided in Sula et al. (2020).

It is also worth adding that, for any given computational cell, the value of \bar{Q} in the energy Eq. (3) is the sum of the right-hand side of (5) and the work of the drag force over all droplets that lie in the cell divided by the volume of the cell. Similarly, the sum of the evaporation rates of the droplets in a cell is equal to the mass exchange rate \bar{T} divided by the cell volume.

As mentioned in the Introduction, the primary breakup of the jet is not directly solved for. Instead, it is taken into account by sampling the parcels according to the Rosin-Rammler size distribution. The secondary breakup of the droplets is modeled using the Modified Taylor Analogy Breakup model described in Sula et al. (2020).

2.2 Combustion Modeling

The FGM method can be considered as the combination of two techniques, the flamelet and the manifold technique. The first one is based on the idea that the multi-dimensional flame structure may be considered as an ensemble of one-dimensional laminar flames. In the context of FGM, its implementation is achieved via the manifold method, according to which a low-dimensional manifold (LDM) is reconstructed numerically by tabulating the chemistry as a function of a limited number of control variables Maas and Pope (1992). Since fluid advection and diffusion processes are represented in one-dimensional flamelets, the FGM provides reasonable accuracy for cold and hot spray regions.

In studies of non-premixed combustion, the corresponding 1D laminar Counterflow Diffusion (CD) flame is often considered as a canonical configuration for the computation of flamelets. According to it, the laminar flamelet equations are expressed in terms of the

spatial coordinate normal to the flame, say x , and time only. Then, the multidimensional character of the flow is taken into account via the local stretch rate $K = \frac{\partial v}{\partial y}$, where v represents the velocity component that is tangential to the stagnation plane and y is normal to the x coordinate Kee et al. (2018). Therefore, the one-dimensional conservation equations for the unsteady CD flames can be written as Stahl and Warnatz (1991); Kee et al. (2018); Long et al. (2018),

$$\frac{\partial \rho}{\partial t} + \frac{\rho u}{\partial x} = -\rho K, \quad (9)$$

$$\frac{\partial \rho Y_i}{\partial t} + \frac{\partial \rho u Y_i}{\partial x} - \frac{\partial}{\partial x} \left(\frac{\kappa}{c_p} \frac{\partial Y_i}{\partial x} \right) = \dot{\omega}_i - \rho K Y_i, \quad (10)$$

$$\frac{\partial \rho h}{\partial t} + \frac{\partial \rho u h}{\partial x} - \frac{\partial}{\partial x} \left(\frac{\lambda}{c_p} \frac{\partial h}{\partial x} \right) = -\rho K h, \quad (11)$$

where $\dot{\omega}_i$ is the chemical source-term of the i -th species Y_i . The local stretch rate K is governed by,

$$\frac{\partial \rho K}{\partial t} + \frac{\rho u K}{\partial x} - \frac{\partial}{\partial x} \left(\mu \frac{\partial K}{\partial x} \right) = \rho_{\text{ox}} a^2 - 2\rho K^2, \quad (12)$$

where ρ_{ox} and a denote the density and prescribed strain rate in the oxidizer stream, respectively. Unity Lewis number is assumed for all species, as heat and species diffusion in spray combustion are dominated by turbulent mixing. This assumption is often invoked in numerical simulations of turbulent combustion of n-dodecane; nonetheless, in the flamelet regime, non-unity Lewis-number effects may be non-negligible.

Dirichlet boundary conditions are specified for the temperature and species mass fractions at the fuel ($x = -L$) and oxidizer ($x = L$) inlets, according to the Spray A configuration; see Table 1 below. Further, for the flame stretch rate, a Dirichlet boundary condition is applied at

Table 1 Case details

Spray details	
Fuel	n-dodecane ($C_{12}H_{26}$)
Fuel temperature [K]	363
Fuel density [kg/m^3]	643
Nozzle diameter [μm]	90
Injection pressure [MPa]	150
Nominal injection velocity [m/s]	550
Injection duration [ms]	1.5
Injected fuel mass [mg]	3.5
Ambient conditions	
Temperature [K]	900
Density [kg/m^3]	22.8
Pressure [MPa]	6

the oxidizer and a zero-Neumann one at the fuel stream. Also, the pressure is kept at 6 MPa, which is the ambient pressure of the Spray A configuration. Finally, the initial condition for the temperature is the mixing profile between the values of the temperature at the two inlets.

It is noted that in spray combustion, the initial temperature of the fuel can be lower than that of the jet because of heat losses due to evaporation. Therefore, in principle, these heat losses should be incorporated in the flamelet equations as is done, for example, in Ma and Roekaerts (2016a, 2016b); Jurić et al. (2021). Nonetheless, Wehrfritz (2016) solved the unsteady flamelet equations for the fuel-oxidizer system in hand by varying the fuel inlet temperature from 250 K to 363 K, the latter being the temperature of the liquid fuel as per the Spray A configuration. According to that study, the fuel inlet temperature had practically no influence on the species composition and played only a minor role in the IDT. Based on these findings, in the present study we opted to construct the FGM database by setting the fuel and oxidizer inlet temperatures to the values provided by the Spray A conditions.

The system of the flamelet Eqs. (9, 10, 11, 12) is closed with the ideal gas law. In our study, its numerical solution is obtained with the one-dimensional flame solver *Ember* Long et al. (2018), while the thermodynamic, transport, and kinetic parameters needed in each equation are computed using the popular package *Cantera* Goodwin et al. (2021).

The LDM is constructed using the steady-state solution of (9, 10, 11, 12) for strain rate a ranging between 1 and 500 s^{-1} , plus one unsteady solution of the flamelet equations for a constant strain rate $a = 500 \text{ s}^{-1}$. The unsteady solution is meant to capture the temporal evolution of the chemical composition from ignition towards the equilibrium steady-state solutions. In non-premixed combustion, it is common to parameterize the LDM in terms of the mixture fraction Z and the reaction-progress variable \mathcal{V} . The mixture fraction governs the mixing between the fuel and the oxidizer, while the progress variable expresses the advancement of the combustion process. Accordingly, a generic flow quantity ψ is expressed as a function of Z and \mathcal{V} , i.e. $\psi = \mathcal{F}_\psi(Z, \mathcal{V})$.

In the present study we have opted for the Bilger definition of the mixture fraction Bilger et al. (1990); Sutherland et al. (2005), which is given in terms of the coupling function ζ as follows,

$$Z = \frac{\zeta - \zeta_0}{\zeta_1 - \zeta_0}, \quad (13)$$

where ζ_1 and ζ_0 are constants evaluated in the fuel and oxidizer stream, respectively. The coupling function ζ is defined in terms of the element mass fractions as

$$\zeta = 2 \frac{Y_C}{W_C} + \frac{1}{2} \frac{Y_H}{W_H} - \frac{Y_O}{W_O}, \quad (14)$$

where W_i denotes the atomic mass of element i .

The reaction-progress variable, \mathcal{V} , is defined as a linear combination of any chemical species that exhibit monotonic behaviour from the initial mixing solution to chemical equilibrium. In the present study, \mathcal{V} is given as a linear combination of three reaction products, namely,

$$\mathcal{V} = \frac{Y_{\text{CO}_2}}{M_{\text{CO}_2}} + \frac{Y_{\text{CO}}}{M_{\text{CO}}} + \frac{Y_{\text{CH}_2\text{O}}}{M_{\text{CH}_2\text{O}}}, \quad (15)$$

where M_i denotes the dimensionless molar mass of the species i ; it is made dimensionless by the molar mass of atomic hydrogen. In this equation, the M_i are to be taken as dimensionless weighting factors, made dimensionless by the atomic mass of hydrogen. The

above definition of \mathcal{Y} has been used in previous studies Wehrfritz et al. (2016); Kahila et al. (2018); Maghbouli et al. (2019) and is based on CH_2O , CO and CO_2 because these species are representative of the initiation, intermediate stages and completion of the combustion, respectively. Generally, there is not a unique way to define the progress variable. In fact, different choices can be selected, depending on the fuel and the chemical kinetics mechanism. Nevertheless, any choice of species is acceptable, and will not impact the results, for as long as it represents all combustion stages and is monotonous from the unburned state to chemical equilibrium. The fulfilment of this criterion must be ensured during the parametrization process.

With respect to LES modeling of turbulent combustion, the flow variables must be formulated as Favre-filtered quantities. A widely used approach is based on the presumed joint Probability Distribution Function (PDF) formulation for the mixture fraction and progress variables,

$$\tilde{\psi} = \int \int \mathcal{F}_{\psi}(Z, \mathcal{Y}) \tilde{P}(Z, \mathcal{Y}) dZ d\mathcal{Y}, \quad (16)$$

where, as mentioned above, $\psi = \mathcal{F}_{\psi}(Z, \mathcal{Y})$ is a generic flow quantity that has been tabulated in the FGM database and \tilde{P} represents the density-weighted joint PDF. In non-premixed combustion, the range of \mathcal{Y} depends on the mixture fraction and takes values between its minimum $\mathcal{Y}_{\min}(Z)$ and equilibrium $\mathcal{Y}_{\max}(Z)$ values. Therefore, it is convenient to normalize \mathcal{Y} and introduce the normalized progress variable $\mathcal{C}(Z)$,

$$\mathcal{C} = \frac{\mathcal{Y} - \mathcal{Y}_{\min}(Z)}{\mathcal{Y}_{\max}(Z) - \mathcal{Y}_{\min}(Z)}. \quad (17)$$

According to Vervisch et al. (2004), Z and \mathcal{C} are only weakly dependent. Thus, as in earlier studies Wehrfritz et al. (2016); Kahila et al. (2018); Zhang et al. (2019), the assumption of statistical independence between Z and \mathcal{C} is also introduced herein, *i.e.* we assume that $\tilde{P}(Z, \mathcal{Y}) = \tilde{P}(Z) \tilde{P}(\mathcal{C})$. Nonetheless, the findings of Vervisch et al. (2004) were based on simulations with single-step chemistry and the validity of this assumption remains a matter of debate. While most of the studies neglect this effect, Meyers and O'Brien (1981) found weak statistical dependency at moderate turbulent Reynolds numbers. As the combustion process occurs far downstream from the injection point, this effect will also be neglected in the current study.

The joint PDF \tilde{P} can be either presumed, *e.g.* parameterized by a limited number of parameters, or computed numerically by solving a balance equation. A widely used approach is to presume that the joint PDF is an analytical function. Different PDFs may be used, and multiple examples of presumed PDFs are available in the literature Borghi (1988); Bray et al. (1989); Ribert et al. (2005); Robin et al. (2006). In the current work, the beta and delta functions are used to approximate the mixture fraction and progress-variable distributions, respectively. Accordingly, the joint PDF simplifies to,

$$\tilde{P}(Z, \mathcal{Y}) = \tilde{P}(Z) \tilde{P}(\mathcal{C}) = \beta(Z; \tilde{Z}, \widetilde{Z''^2}) \delta(\tilde{\mathcal{C}} - \mathcal{C}). \quad (18)$$

It is acknowledged that assuming a delta-function distribution for the scaled progress variable \mathcal{C} amounts to neglecting the influence of turbulent fluctuations in the advancement of the combustion process. Strictly speaking, this is true only for the case of infinitely fast chemistry. Nonetheless, for the purposes of our study, we may assume that the chemical reactions are fast enough so that the introduction of a delta-function distribution is still

acceptable. An improvement of this approach would be to consider a beta-function distribution for \mathcal{C} and further introduce its variance \mathcal{C}''^2 as an additional control variable in the construction of the FGM database. This methodology may capture the turbulence-chemistry interaction more accurately, which is a topic of our current investigations.

As is typical in LES of variable-density flows, the transport equations for the mixture fraction and the progress variable are also spatially filtered, yielding the following equations for the corresponding Favre-averaged quantities, \tilde{Z} and \tilde{Y} ,

$$\frac{\partial \bar{\rho} \tilde{Z}}{\partial t} + \nabla \cdot (\bar{\rho} \tilde{u} \tilde{Z}) = \nabla \cdot (\bar{\rho} \tilde{u} \tilde{Z} - \bar{\rho} \tilde{u} \tilde{Z}) + \nabla \cdot (\bar{\rho} \bar{D} \nabla \tilde{Z}) + \bar{S}_Z, \tag{19}$$

$$\frac{\partial \bar{\rho} \tilde{Y}}{\partial t} + \nabla \cdot (\bar{\rho} \tilde{u} \tilde{Y}) = \nabla \cdot (\bar{\rho} \tilde{u} \tilde{Y} - \bar{\rho} \tilde{u} \tilde{Y}) + \nabla \cdot (\bar{\rho} \bar{D} \nabla \tilde{Y}) + \bar{\omega}_Y. \tag{20}$$

In the above equations, \bar{S}_Z represents the spray source term. for a single-component fuel; it is equal to the mass source term in (1), $\bar{S}_Z = \bar{\Gamma}$. Also, $\bar{\omega}_Y$ represents the chemical source term is obtained from the FGM database. The unresolved turbulent fluxes resulting from spatial filtering of the equations are modeled via a gradient assumption, *i.e.* in the same fashion as the unresolved turbulent flux in the energy equation (3). Herein it is assumed that the turbulent Schmidt number is equal to unity.

Lastly, the subgrid variances of mixture fraction are estimated using the algebraic model proposed by Pierce and Moin (1998),

$$\widetilde{Z''^2} = \widetilde{Z}^2 - \tilde{Z}^2 = C_{v,Z} \Delta^2 \left| \frac{\partial \tilde{Z}}{\partial x_j} \right|^2. \tag{21}$$

where $C_{v,Z}$ represents the model constant which is dynamically evaluated according to the process described Balarac et al. (2008) and Δ denotes the LES filter width.

The coupling between the FGM database and the LES spray solver is achieved via a representative set of species and the source terms in (20) and (3) which are stored functions of \tilde{Z} , \tilde{C} and $\widetilde{Z''^2}$. The composition of the mixture is determined through the lookup procedure from the FGM database. Thus, no transport equation for any species mass fraction is solved. In our implementation of this procedure, five major species are considered out of all the species that are present in the respective chemical mechanism, namely, $C_{12}H_{26}$, O_2 , CO_2 , H_2O and N_2 . We remark that in reaction zones, where many intermediate species are present, the sum of the concentrations of these five species is not unity after the onset of combustion. For this reason, the mass fraction of N_2 is calculated on the basis of the mass fractions of the other four species, thereby enforcing that the sum of the mass fractions of the five dominant species is equal to unity. In principle, this simplification may have an impact in the computation of the mixture density because the latter is calculated via the thermal equation of state which involves the mixture composition. However, in preliminary tests that we conducted in the context of our study, the error in the density due to this simplification was found to be less than 2%, which is deemed acceptable for the purposes of our simulations.

The energy equation in the LES spray solver is cast in terms of the sensible enthalpy and reads,

$$\frac{\partial(\tilde{\rho}\tilde{h}_s)}{\partial t} + \nabla \cdot (\tilde{\rho}\tilde{h}_s\tilde{\mathbf{u}}) = -\frac{1}{2}\frac{\partial(\tilde{\rho}|\tilde{\mathbf{u}}^2|)}{\partial t} - \frac{1}{2}\nabla \cdot (\tilde{\rho}|\tilde{\mathbf{u}}^2|\tilde{\mathbf{u}}) + \frac{\partial\tilde{p}}{\partial t} + \nabla \cdot ((\tilde{\mu} + \mu_t)\tilde{\mathbf{V}}^d\tilde{\mathbf{u}}) + \nabla \cdot \left(\left(\frac{\tilde{\kappa}}{\tilde{c}_p} + \frac{\kappa_t}{c_p} \right) \nabla\tilde{h}_s \right) + \tilde{S}_h + \tilde{Q}. \quad (22)$$

Then, the temperature field is computed via an approximation of the filtered heat capacity of the mixture, on the basis of the aforementioned five species. As mentioned in the Introduction, the basic advantage of this approach is that it does not require precise knowledge of the entire composition of the mixture, thereby reducing the workload and memory requirements of the numerical simulation. An additional advantage is that it accounts seamlessly for the cooling effect due to evaporation. On the other hand, it carries over the error in the representation of the mixture composition. However, as mentioned above, the induced error in the density was found to be quite small. A similar approach for approximating the transport properties of the mixture was successfully applied in earlier studies Kahila et al. (2018); Payri et al. (2019); Jurić et al. (2021).

The tabulated variables in the FGM database that are required to solve the governing equations are the source term \tilde{Q} of Eq. (22), the source term $\tilde{\omega}_j$ of Eq. (20), and the mass fractions of $C_{12}H_{26}$, O_2 , CO_2 , and H_2O . The database is constructed from $161 \times 141 \times 21$ data points for the mixture fraction, scaled progress variable, and mixture fraction variance. The data points for the mixture fraction are unevenly spaced and clustered around the stoichiometric values. By contrast, the data points for the mixture fraction variance are evenly distributed throughout its range. Additionally, the points for the scaled progress variable are refined towards the high and lower values so as to properly capture the initiation and completion of the combustion. The basic tabulated quantities are the source terms in the energy (3) and progress variable (20) equations, as well as the mass fractions of the aforementioned five species upon which the computation of the thermophysical properties of the gas is based. Also, additional quantities that are used in the post-processing of the results, such as OH and H_2O_2 concentrations, are also tabulated.

2.3 Chemical Kinetics Mechanisms

As mentioned above, the ECN spray A operating condition xxx (2021) uses n-dodecane as a surrogate for Diesel fuel. Due to the large number of species and reactions involved in the oxidation of n-dodecane, numerical studies are typically based on reduced mechanisms. Selecting a suitable kinetics mechanism plays a crucial role in reacting flow simulations, since the emerging patterns and global properties of the flow are mechanism dependent.

In the present study, we employ two popular mechanisms for the oxidation of n-dodecane: the 255-species/1524-reaction mechanism of Narayanaswamy et al. (2014) and the 130-species/2395-reactions mechanism of Ranzi et al. (2014). They were derived from different detailed kinetic mechanisms Sarathy et al. (2011); Ranzi et al. (2012), using reduction strategies such multi-stage automatic species, reaction elimination and chemical lumping of species. For a detailed description of the reduction procedures, the reader is referred to the aforementioned original publications. According to their authors, the mechanisms Narayanaswamy et al. (2014) and Ranzi et al. (2014) are valid for both low and high temperature combustion and are well suited for capturing ignition delay times. Following the

nomenclature of Wehrfritz et al. (2016), the mechanisms Narayanaswamy et al. (2014) and Ranzi et al. (2014) will be henceforth referred to as *Stanford* and *Polimi*, respectively.

3 Computational Setup

According to the ECN Spray A operating condition xxx (2021), n-dodecane is injected into stationary gas through a nozzle whose orifice diameter is 90 μm . The initial temperature and density of the stationary gas are 900 K and 22.8 kg/m^3 , respectively. In our setup, the initial velocity of the droplets is calculated from the injected mass flow rate, while the injection direction is chosen randomly within the prescribed spray cone of the ECN Spray A operating condition. Additionally, the initial droplet diameter of the parcels follows from the Rosin-Rammler distribution with parameters that lead to an initial Sauter mean diameter of 6 μm . The initial molar composition of the gas is: $[\text{N}_2]=75.15\%$, $[\text{CO}_2]=6.23\%$, $[\text{H}_2\text{O}]=3.62\%$ and $[\text{O}_2]=15\%$, where the brackets denote molar fractions. Moreover, the initial thermodynamic conditions for our simulations are listed in Table 1.

The computational domain is a cuboid whose streamwise length is 80 mm and cross-section is 20 mm \times 20 mm. The walls are assumed to be rigid and adiabatically isolated. The domain is discretized with a fully hexahedral mesh and refined via a cell-splitting approach in the high-velocity and spray-ignition regions. Five levels of refinement are used. The smallest cell size is 40 μm and is used in the vicinity of the injection point and the dense-spray region (black region in Fig. 1). This value satisfies the guidelines of Xue et al. (2013) according to which, for a good quality LES of the Spray A configuration, the cell size in the dense-spray region may not exceed 60 μm . At the next level of refinement, the cell size is 80 μm (grey region); this value is determined on the basis of our earlier cold spray flow simulations Sula et al. (2020). In the next region, the cell size is set at 160 μm (light grey region). Then, a transition layer of five cells of 320 μm each is employed. Finally, the largest cell size is 640 μm and corresponds to the white region of Fig. 1. The extent of the various refinement regions is based on preliminary simulations that we conducted in the context of our study and on a sensible trade off between accuracy and computational cost. The resulting mesh is composed of 11.8 million cells.

For all simulations, we use a variable timestep with a CFL number equal to 0.3. Finally, the end-time of the simulation is set to 1.6 ms.

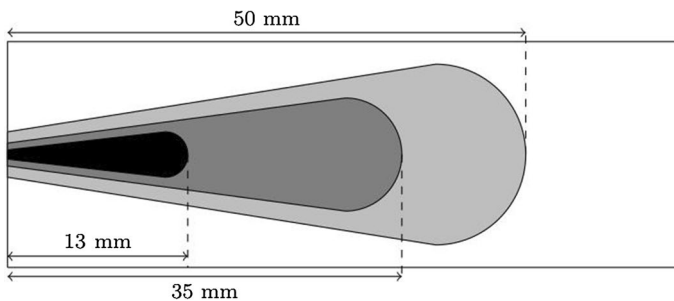


Fig. 1 Computational mesh with refinement regions. Cell sizes: white region 640 μm ; light grey region 160 μm ; grey region 80 μm ; black region 40 μm . The five-cell transition layer between the white and light grey region is not shown for visibility purposes

4 Results and Discussion

4.1 Flamelet Solution

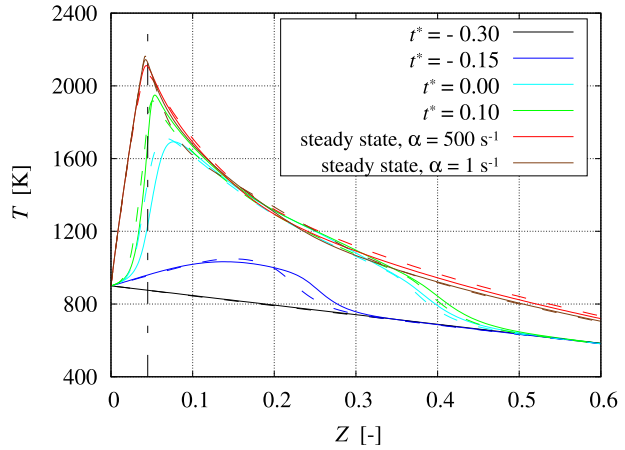
The FGM database is obtained by combining the solution of the unsteady flamelet Eqs. (9, 10, 11, 12) for a constant strain rate $\alpha = 500 \text{ s}^{-1}$ and multiple steady-state flamelet solutions at strain rates ranging from $\alpha = 1$ to 500 s^{-1} . According to Wehrfritz (2016), a single unsteady solution is sufficient to capture the ignition of the mixture and the transition to the steady-state solution. Further, the author of Wehrfritz (2016) computed unsteady flamelet solutions over a variety of strain rates and reported that in CD flames and for $\alpha < 1000 \text{ s}^{-1}$, the IDT became insensitive to the strain rate and, furthermore, the strain rate had only a small effect on the species composition during the early onset of ignition. Based on these findings, we have adopted herein the same strategy for constructing the FGM database. Nonetheless, it is important to mention that these findings of Wehrfritz (2016) concern the specific ECN Spray A conditions and may not be valid for different conditions or fuels.

Another point of caution is that, when constructing the FGM database, we must assure that there is a smooth transition between unsteady and steady solutions in the $Z - C$ space. To this end, the transition from the unsteady to the steady solutions is achieved via interpolation. Finally, in regions where the steady and unsteady solutions overlap, then the unsteady ones are selected over the steady ones. It should be noted that the maximum of the progress variable after ignition slightly exceeds the steady-state value. Beyond this maximum, the progress variable decreases and reaches its steady-state value as the flamelet solution approaches that of chemical equilibrium. This part is omitted when constructing the FGM database so as to ensure the monotonicity of the progress variable, hence a consistent database.

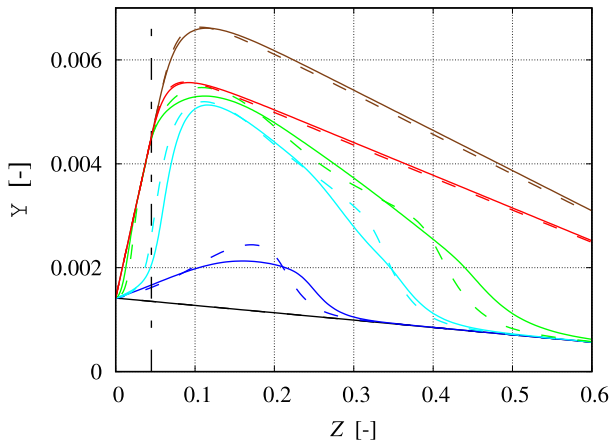
Multiple definitions for the IDT have been used in previous studies Wehrfritz et al. (2016); Tekgül et al. (2020) or within the ECN xxx (2021). Nevertheless the predicted value is largely insensitive to their definitions. In our analysis the IDT is defined as the time when the mass fraction of OH reaches 2% of its steady-state value. According to this definition, the IDT for CD flames resulting from the Polimi and Stanford mechanisms are 0.30 ms and 0.39 ms, respectively. In other words, the difference in the ignition delay between the two combustion mechanisms is 0.09 ms. It is noted that the IDT in spray combustion is expected to be shorter than in laminar CD flames, mainly due to the flow turbulence which enhances mixing.

Figure 2 shows plots of the temperature and progress variable as functions of Z and at times t^* shifted relative to the IDT, *i.e.* $t^* = t - \text{IDT}$. The results of the unsteady CD flames show good agreement between the two mechanisms. For the Stanford mechanism, the mixture requires more time to ignite, but the temperature profile matches that of the Polimi mechanism after its ignition. Also, from these plots we confirm the monotonicity of the progress variable, which is an important condition for capturing the transition from the unburned to the fully burned state. We further confirm the convergence of the unsteady solution to the steady one near Z_{st} and for high values of \mathcal{Y} , which also implies compatibility of the steady and unsteady solutions for the mass fractions of the major combustion species. For both combustion mechanisms, the maximum temperature is reached at the stoichiometric value, while the peak of the progress variable is attained in the rich-mixture region, $Z > Z_{\text{st}}$.

Fig. 2 Evolution of **a** temperature T and **b** progress variable \mathcal{Y} as functions of mixture fraction Z , from unsteady flamelet solution for strain rate $\alpha = 500 \text{ s}^{-1}$, at times t^* shifted relative to the IDT. Solid lines mark the Polimi mechanism and dashed lines the Stanford one. The vertical dashed line denotes the stoichiometric mixture fraction Z_{st} . The legend in **b** is the same as in **a**



(a) Temperature (T)



(b) Progress variable (\mathcal{Y})

In Fig. 3 we provide plots of the source term $\dot{\omega}_y$ of the progress variable Eq. (20) and the source term \bar{Q} of the energy equation. The source term $\dot{\omega}_y$ controls the advancement of the combustion process hence the numerical prediction of the IDT. Concerning the differences between the two mechanisms, from the plots it can be inferred that Polimi yields higher values for $\dot{\omega}_y$ in the region of low \mathcal{Y} , more specifically in the range $\mathcal{Y} = 0.001 - 0.002$. This region represents the early onset of combustion and, therefore, the difference in $\dot{\omega}_y$ contributes directly to the aforementioned difference in the prediction of the IDT. Moreover, for $\mathcal{Y} > 0.002$, the Stanford predictions for $\dot{\omega}_y$ are higher than the Polimi ones. Regarding the heat of combustion \bar{Q} , high values are attained in the rich-fuel mixture region for both mechanisms. It is worth observing that, close to the stoichiometric conditions and for $\mathcal{Y} \approx 0.0045$, there is a small region where \bar{Q} attains quite high values. Overall, these plots suggest that the combustion process in the CD flame configuration occurs under rich conditions.

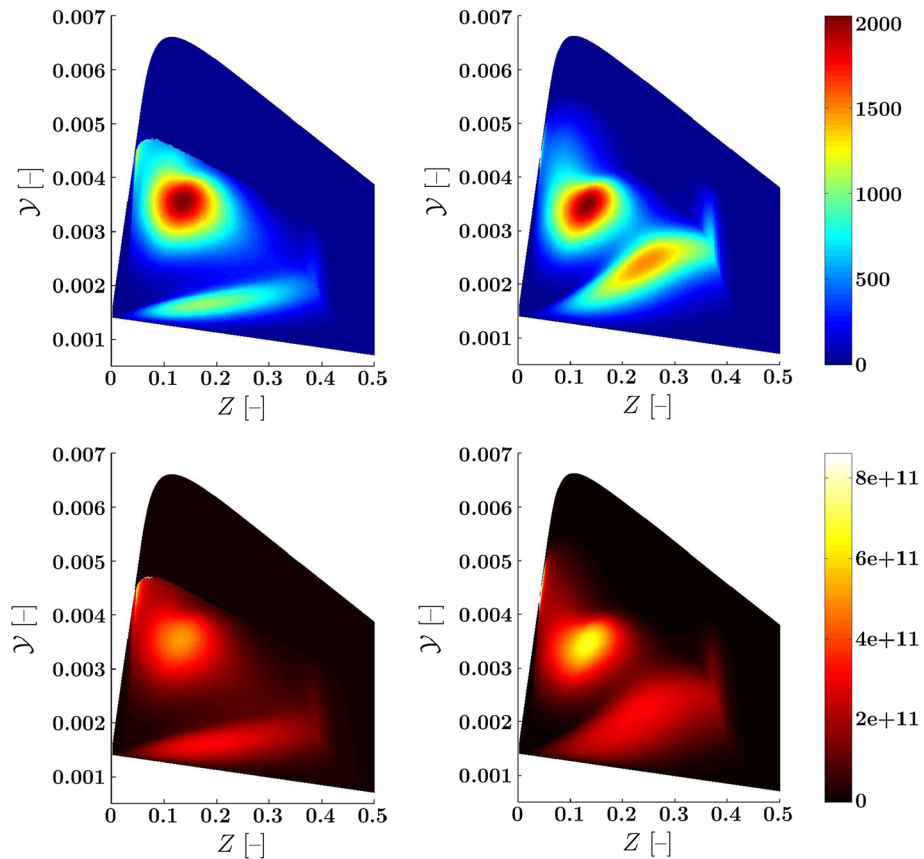


Fig. 3 Distributions of the source term $\dot{\omega}_y$ (first row) and heat of combustion \bar{Q} (second row) as functions of Z and Y , according to the Polimi (first column) and Stanford (second column) mechanisms. (For interpretation of the references to color in this figure legend, the reader is referred to the electronic version of this article.)

4.2 Computational Cost and Memory Requirement of the LES

The flamelet solution are integrated and the results are then converted into the FGM database. In our implementation, the FGM database consists of 9 tables, each containing $161 \times 141 \times 21$ entry points. The tables are the mass fractions of five dominant species, two source terms for the progress-variable and energy equations, plus the quantities $Y_{\min}(Z)$ and $Y_{\max}(Z)$ that are necessary to calculate the scaled progress variable C from Eq. (17).

Since a double-precision scalar in OpenFOAM occupies 64 bits or, equivalently, 7.63×10^{-6} MB, the memory needed to store the FGM database would be 3.64 MB. In a typical computer cluster, this will result in an additional 3.64 MB per core. This is because OpenFOAM uses the domain decomposition method in parallel computations; therefore, each decomposed domain is required to load the entire FGM database. Our LES study was carried out on a parallel cluster with scalable processors (Intel® Xenon® 6248, 2.50 GHz). The computational cost of the reactive Spray A using a mesh of 11.8 million cells is approximately 2400 CPU hours. Overall, and taking into account the complexity of turbulent spray

combustion, the computational cost of our LES-FGM methodology is considered to be satisfactory and encouraging for possible application to engine simulations.

4.3 Spray Ignition and Temporal Evolution of the Flame

In this section, we present results for the spray ignition, and the temporal evolution and global properties of the flame. The differences in the predictions of the IDT and FLOL with the two combustion mechanisms are also discussed.

Initially, when the liquid fuel is injected into the combustion chamber, the dominant physical phenomena are the breakup of the droplets and the subsequent liquid fuel evaporation. Consequently, in absence of combustion, the instantaneous temperature distribution in the injection region is similar with both mechanisms. These similarities can clearly be seen in Fig. 4 which shows color-filled plots of the temperature at the central plane and at different time instances. The temperature decrease observed in this region, $z < 10$ mm, is due to interphasial heat exchange and droplet evaporation. As the spray develops and the fuel vapor mixes with the air downstream, an amount of heat is released due to combustion in the fuel-rich part of the spray which raises the temperature by 200 – 300 K. This phenomenon occurs at $t \approx 0.2$ ms with the Polimi mechanism and $t \approx 0.3$ ms with the Stanford mechanism, and signals the onset of the low-temperature combustion, also known as “first-stage ignition”.

According to our simulations, the second-stage ignition occurs in the low-velocity region close to the tip and at the periphery of the vapor spray. During this stage, multiple self-igniting kernels are formed almost simultaneously inside this region, as it can be observed from Fig. 4. We may therefore assume that the reactions occurring therein provide the necessary heat release to promote low-temperature combustion throughout the entire spray. This sequence of events during the second-stage ignition were also observed in previous experimental and numerical studies of spray combustion Oldenhof et al. (2010); Skeen et al. (2015); Kahila et al. (2018). The temperature field with the Polimi mechanism at $t = 0.3$ ms that is shown in Fig. 4 is representative of this stage. With regard to the Stanford mechanism, representative temperature distributions of this stage are those at $t = 0.3$ and 0.4 ms. We may therefore conclude that the Stanford mechanism predicts that the second-stage ignition occurs later than the Polimi mechanism does. After this stage, the high-temperature region expands in all directions and the flame stabilizes at the FLOL, as it can be inferred from plots at $t = 0.6$ ms in Fig. 4. In other words, at a later stage, the mixture undergoes a high-temperature volumetric ignition.

The various ignition stages can be observed in Fig. 5, which shows plots of the temporal evolution of the maximum temperature in the computational domain. The profiles obtained with the two mechanisms are very similar; for example, they agree very well in the predictions for the rate of temperature increase and for the temperature of the combustion products during the ‘quasi-stationary’ state of volumetric expansion of the flame for $t > 0.6$ ms. In fact, the LES predictions for the temperature at this stage, around 2220 K, are very close to that of the CD flames and exceed it by only 2 to 4%. A priori, there is no reason for these values to coincide. The fact that they are close implies that the turbulence-chemistry interaction is not very strong. Also, the most noticeable difference between the two profiles is that the Stanford mechanism predicts a longer ignition delay by approximately 0.1 ms. In other words, there is an offset of about 0.1 ms between the two profiles of the maximum temperature.

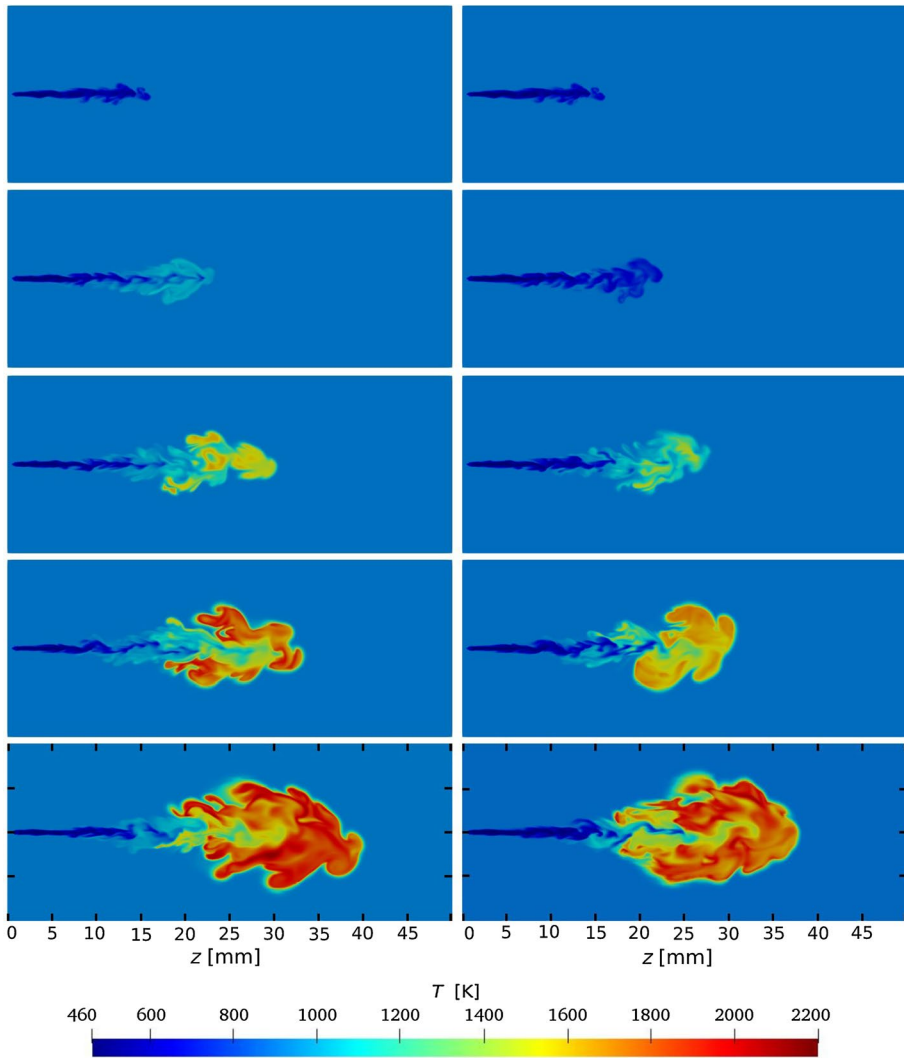


Fig. 4 Color-filled plots of the temperature T at the central vertical plane using the Polimi (left) and Stanford (right) mechanisms, at times $t = 0.1, 0.2, 0.3, 0.4$ and 0.65 ms

For comparison purposes, we have also plotted the corresponding profiles from Wehrfritz et al. (2016). Once again, the profiles are very similar, but those from Wehrfritz et al. (2016) predict a longer ignition delay by approximately 0.15 ms. Another difference is that our simulations predict small-scale fluctuations of the temperature during the ‘quasi-stationary’ state. These fluctuations are attributed to the flow turbulence. However it is conceivable that their amplitude gets accentuated due to errors in the computation of the heat capacity of the mixture which is computed on the basis of the five major species of the combustion process. However, an increase of the number of species used in this computation would result in a significant increase of the computing time.

Fig. 5 Maximum temperature evolution in the computational domain along with numerical results of Wehrfritz et al. (2016)

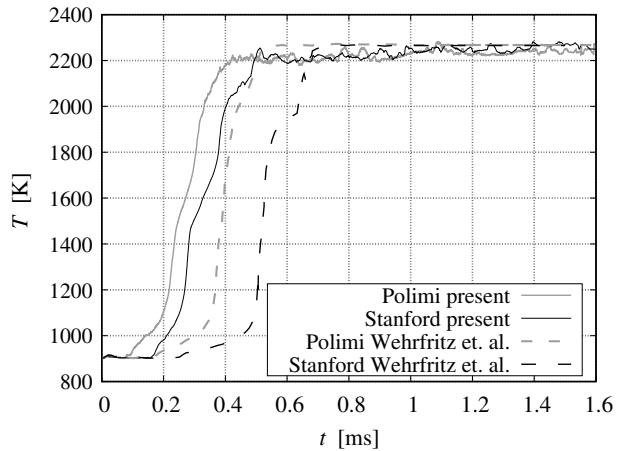


Figure 6 shows the distribution of the scaled progress variable C in the computational domain and at different time instances. Qualitatively, the predictions from the two mechanisms are similar. However, at all times, the Polimi mechanism predicts higher values in the region close to the nozzle. This implies an earlier onset of the combustion process, thereby leading to earlier ignition and shorter IDT. By contrast, with the Stanford mechanism, ignition is delayed longer and occurs at a larger distance from the injection nozzle, as it can be inferred upon comparison of the plots at $t = 0.1$ ms and 0.2 ms. From the plots at these time instances we can also observe that the mixture initially ignites at the front of the jet. It also is worth observing the volumetric ignition at $t = 0.65$ ms which takes place within multiple ignition kernels. According to these plots, the maximum values of C are attained at the periphery of the spray.

We proceed to discuss the predictions of our simulations for the IDT and FLOL. In experiments, the IDT and FLOL are typically determined from the excited state of OH. However, in numerical studies, the 2% OH guideline is often applied. More specifically, following the ECN guidelines xxx (2021), the definition of IDT employed herein is the first time instance at which the mass fraction of OH reaches 2% of its peak value, throughout the computational domain, once a stable flame is established. Also, the FLOL is determined as the first axial location of the OH mass fraction reaching 2% of its maximum value in the domain.

In Fig. 7 we have plotted our numerical predictions for the IDT and FLOL (with both mechanisms), together with the numerical results of Wehrfritz et al. (2016) and the experimental data of Sandia Lillo et al. (2012), TU/e Maes et al. (2016) and IFPEN xxx (2021). We observe that our predictions for the FLOL, with both mechanisms, are in good agreement with the experimental data. With regard to the IDT, our LES results are 0.28 ms with the Polimi mechanism and 0.34 ms with the Stanford one, whereas the experimental data of Sandia, IFPEN and TU/e are, respectively, 0.44, 0.4 and 0.41 ms. In other words, the LES underpredict the IDT. Also, our results for the IDT are considerably different than those in Wehrfritz et al. (2016); the discrepancy may be attributed to the different FGM implementations and droplet breakup models. On the other hand, our results are in good agreement with the numerical studies Davidovic et al. (2017); Tekgül et al. (2020). It is also noted that our LES predictions are slightly shorter than the IDT of CD flames mentioned above, presumably due to turbulence. In other words,

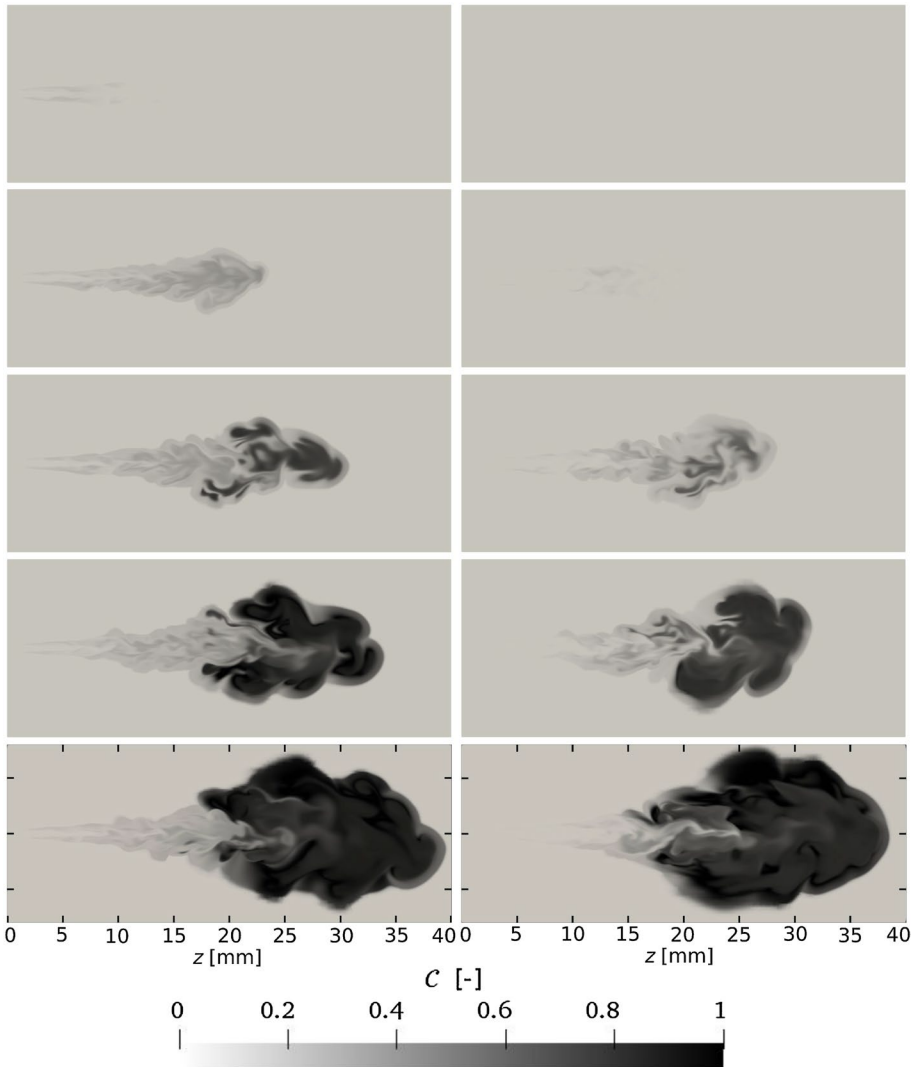


Fig. 6 Color-filled plots of the scaled progress variable, C , at the central vertical plane using the Polimi (left column) and Stanford (right column) mechanisms, at times $t = 0.1, 0.2, 0.3, 0.4$ and 0.65 ms

the LES predictions for the IDT appear to be consistent with the data provided in the FGM database.

4.4 Temperature and Species Mass-Fraction Distributions

In this section we elaborate further on the properties of the temperature field and also discuss the distributions of the mass fractions of formaldehyde CH_2O , hydroxyl OH , and hydrogen peroxide H_2O_2 . The objective is to further explore the flame characteristics, as predicted with the two kinetics mechanisms, and to make comparisons with experiments.

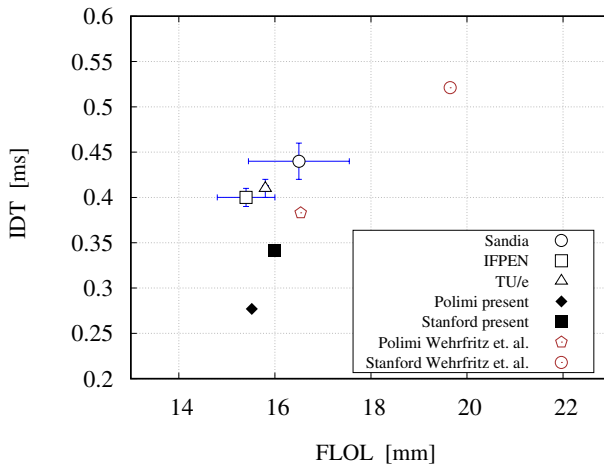


Fig. 7 Numerical and experimental results for the Ignition delay time (IDT) and flame lift-off length (FLOL). The numerical results are those of the present study and of Wehrfritz et al. (2016). The experimental data are those of Sandia Lillo et al. (2012), TU/e Maes et al. (2016) and IFPEN (2021). The error bars indicate the standard deviation in the experimental data

To this end, we first investigate the temperature and CH_2O distributions in Z space. The computational domain is divided in 4 distinct regions in terms of the axial distance from the injection point z , namely $z < 10$ mm, $10 \leq z < 20$ mm, $20 \leq z < 30$ mm, and $z \geq 30$ mm. The LES results for the temperature and formaldehyde mass fraction are then sampled at different time instances in each of these 4 regions. It is noted that sample points with $Z < 0.001$ are not included in this analysis.

Figure 8 shows scatter plots of T against Z at different time instances, for each region identified above. According to these plots, at $t = 0.1$ ms, liquid fuel evaporation and mixture formation are dominant close to the injection point. This is evidenced by the presence of the adiabatic mixture line along which T attains lower values for higher values of Z . Additionally, it can be observed that only a small fraction of the vaporized fuel deviates from the adiabatic mixing conditions.

The evolution of the temperature during the ignition process can also be inferred from the scatter plots in Fig. 8. The most striking feature at early times is that the temperature distribution begins to scatter much earlier when the Polimi mechanism is used, which evidently indicates lower IDT. Further, on the basis of the temperature peaks at $t = 0.25$ ms (Polimi) and $t = 0.3$ ms (Stanford), we infer that ignition takes place in the third region of the domain, $20 \leq z < 30$ mm, and at fuel-rich conditions: $Z = 0.1$ with Polimi mechanism and $Z = 0.14$ with the Stanford one. Once the mixture is ignited, the temperature rises rapidly and its peak shifts towards the stoichiometric value, $Z_{st} = 0.045$. At the same time, the scattering of the temperature distribution spreads. At $t \approx 1.5$ ms, when the flame has already expanded and has reached a ‘quasi-stationary’ state the temperature plots with the two mechanisms are quite similar both in the high and low-temperature regions. Moreover, for any given value of Z for which combustion occurs, the temperature peak is located in the fourth region of the domain, $z > 30$ mm, depicted by red dots in the plots. Also, the global maximum of the temperature is reached very close to the stoichiometric value.

In Fig. 9 we present the time-averaged temperature distribution along the spray axis (averaged between $t = 1$ ms and 1.6 ms). According to these plots, the temperature drops

Fig. 8 Scatter plot of temperature against mixture fraction, obtained with the Polimi (left) and Stanford (right) mechanisms. (For the interpretation of the references to color in this figure legend, the reader is referred to the electronic version of this article.)

rapidly and in a linear fashion away from the injection point. For example, at $z = 2.5$ mm it has already dropped by approximately 400 K. This drop is due to the energy consumed for the heating and evaporation of the liquid fuel. Past this point, the temperature rises and we may identify three different zones of increase. For $2.5 < z < 15$ mm, T rises at a moderate rate. For $15 < z < 25$ mm, T rises at a very high rate, almost by 1000 K. This region signals the transition from low to high-temperature combustion. In the third zone, $z > 25$ mm, the increase rate is again moderate and similar to that of the first zone. We further observe that the temperature distribution exhibits some oscillations, presumably due to turbulence. It is also interesting to note that the profiles predicted by the two mechanisms are very close to one another.

An essential feature of high-temperature oxidation of hydrocarbons is the progressive formation of formaldehyde. In fact, CH_2O is the key species that characterized the transition from low to high-temperature combustion Klein and Schoen (1958). According to our numerical results, the FLOL is between 15 and 17 mm. Therefore, this region should be characterized by high CH_2O concentration. In Fig. 10 we present scatter plots of the CH_2O mass fraction at different time instances, namely, $t = 0.2, 0.25, 0.3,$ and 0.4 ms. From these plots we can observe that the peaks of the CH_2O mass fraction occur principally in the region $10 < z < 20$ mm (corresponding to black dots in the plots) which encompasses the FLOL. It is also noted that, according to the Polimi mechanism, the distribution of the CH_2O mass-fraction retains the same shape at all times. The peak value stays more or less constant, $Y_{\text{CH}_2\text{O}} \approx 0.015$ and occurs for $Z \approx 0.2$. The shape of the CH_2O distribution according to the Stanford mechanism also remains the same but is steeper. Further, its peak value is 0.02 and occurs at $Z \approx 0.25$. Finally, the simulations with both mechanisms predict that at $t = 0.4$ ms, CH_2O is present at larger distances, $z > 30$ mm. This however is mostly due to advection and species diffusion and secondarily due to chemical reactions.

Next, in Fig. 11 we present color-filled plots of the CH_2O mass fraction at the central vertical plane and different time instances, juxtaposed with the experimental data of Skeen et al. (2015). The time instances that these plots are taken are shifted relative to the corresponding IDT; in other words, they are presented in terms of $t^* = t - \text{IDT}$. Overall, the predictions with the two mechanisms for the temporal evolution of the CH_2O are similar. Further, the LES results agree well with the experimental data with regard to the area in which the CH_2O concentration is high. Nonetheless, between the two mechanisms, there are some differences in the predictions of the spatial distribution of CH_2O . Most noticeably, with the Polimi mechanism, CH_2O starts to form at a certain distance from the injection point, $z > 10$ mm, in accordance with the experimental data. On the other hand, with the Stanford mechanism, CH_2O starts to form much closer to the injection point, which is not observed in the experiments.

Another important species that is often gauged in both experimental and numerical studies is the hydroxyl OH. This is so because high OH concentrations correspond to regions of combustion at high temperature. It is therefore interesting to examine how the LES results for the OH distribution compare to experimental data. To this end, in Fig. 12 we present color-filled plots of the OH mass fraction at the central vertical plane and $t = 1.5$ ms, juxtaposed with the experimental data of Maes et al. (2016). Those data were obtained via the Planar Laser-Induced Fluorescence (PLIF) optical-diagnostics technique. From the plots

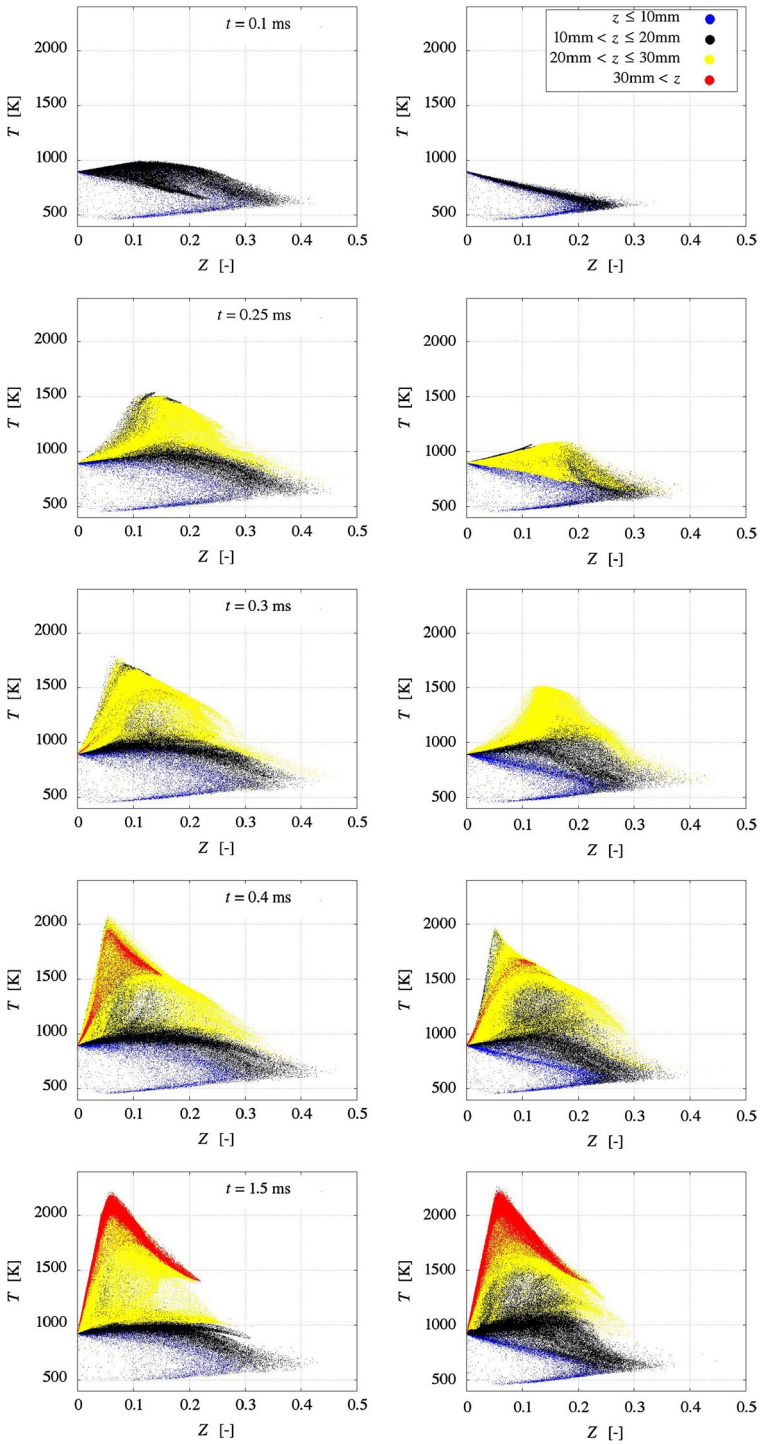
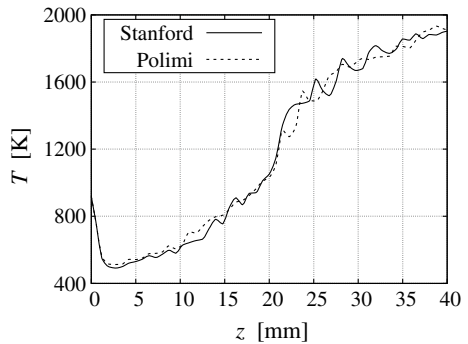


Fig. 9 Average temperature along the spray axis between $t = 1$ ms and 1.6 ms



we can infer that the LES predictions for the location and shape of the regions with high OH concentration agree reasonably well with the experimental measurements. One point of discrepancy is that, the experimental data show high OH concentration in the vicinity of the FLOL, whereas the LES results indicate a slightly decreased value therein.

We conclude with a discussion on the concentration of hydrogen peroxide, H_2O_2 . This species has unique combustion characteristics; for example, it can be used as a bipropellant when combined with other fuels. In such cases, H_2O_2 acts as an oxidizer, and its presence can significantly facilitate the oxidation process of other fuels Li and Wei (2016); Gribi et al. (2018). The dual nature of H_2O_2 as fuel and oxidizer carries potential benefits in clean-combustion technology because it contributes to reducing NO_x and CO_2 emissions. It is therefore useful to examine the numerical predictions on the formation and consumption of this species. To this end, in Fig. 13 we present plots of the mass fraction of H_2O_2 at the central vertical plane and at different times relative to the corresponding IDT, $t^* = t - IDT = -0.1, -0.05, 0$ and 0.05 ms. Globally, we discern two stages relative to its formation and consumption. In the first stage, represented by the plots at $t^* = -0.1$ and -0.05 ms, H_2O_2 is formed before ignition at low temperatures and over the entire spray region. The second stage occurs after ignition, and is characterized by consumption of H_2O_2 at the regions of high-temperature combustion plus continued formation of it at the low-temperature regions. Overall, the numerical results for the temporal evolution and spatial distribution of H_2O_2 with the two mechanisms are quite similar, especially with regards to the second stage.

Overall, on the basis of the results presented herein, we may conclude that even though the simulations with the two mechanisms predict different IDT, the results for flow properties in the later stages of the combustion process are quite similar.

5 Concluding Remarks

In this article, we presented a numerical study of the n-dodecane spray flame under the ECN Spray A operating condition. In our simulations we employed the LES approach, coupled with the Flamelet Generated Manifolds (FGM) methodology for combustion modeling. Also, the breakup of the droplets was modeled via the so called Modified Taylor Analogy Breakup model Sula et al. (2020). With regard to the coupling between the FGM database and the LES equations, the energy equation is cast in terms of the sensible enthalpy and contains a source term for the heat release that is computed directly from the

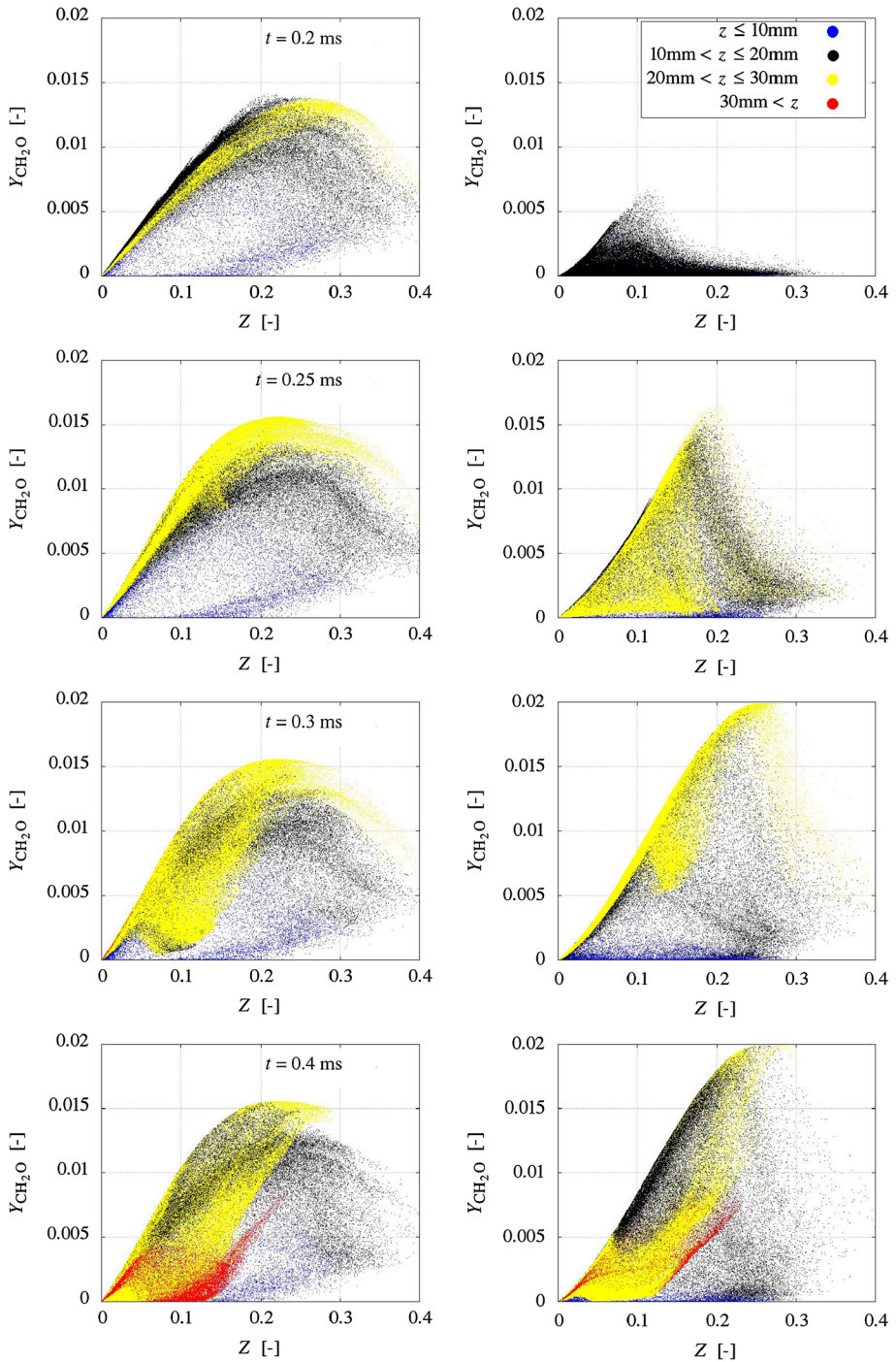


Fig. 10 Scatter plot of CH_2O mass fraction against mixture fraction with the Polimi (left) and Stanford (right) mechanisms. (For the interpretation of the references to color in this figure legend, the reader is referred to the electronic version of this article.)

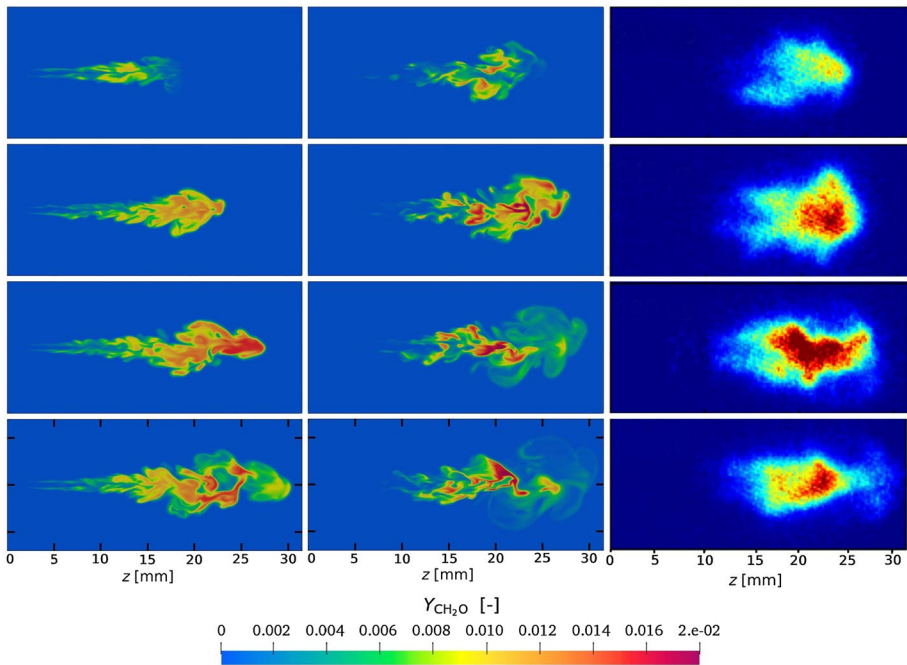


Fig. 11 Color-filled plots of CH_2O mass fraction at the central vertical plane distribution and times $t^* = t - \text{IDT} = -0.1, -0.05, 0, 0.05$ ms, for the Polimi (left) and Stanford (center) mechanisms, together with the experimental PLIF data from Skeen et al. (2015). The attached colormap does not apply to the experimental data. (For the interpretation of the references to color in this figure legend, the reader is referred to the electronic version of this article.)

database. Then, for the computation of the temperature, the specific heat of the mixture is approximated on the basis of five major species. This procedure results in significant computational savings without sacrificing the fidelity of the computations.

Simulations were carried out with two popular chemical kinetics mechanisms and the numerical results were compared against available experimental data and previous numerical studies. According to them, the proposed LES-FGM coupling can accurately capture the various stages of the evolution of the reactive spray, namely, droplet evaporation and breakup, mixture formation, first and second-stage ignition, and volumetric flame expansion. Compared against experimental data, the simulations predicted quite accurately the

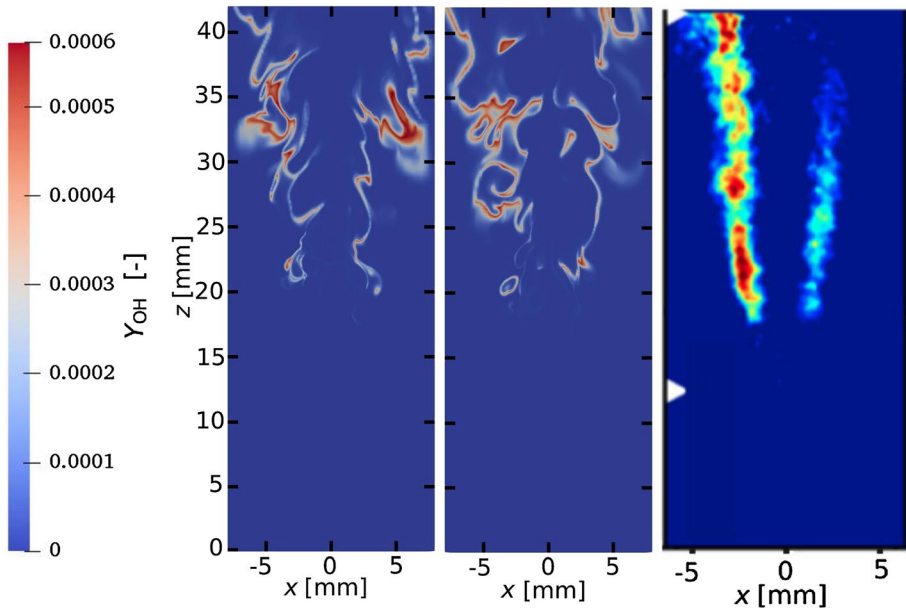


Fig. 12 Color-filled plots of OH mass fraction at the central vertical plane, with the Polimi (left) and Stanford (center) mechanisms, along with the experimental PLIF data from Maes et al. (2016) (right). The LES results are taken at $t = 1.5$ ms. The attached colormap does not apply to the experimental data

FLOL but underpredicted the IDT. Nevertheless, the numerical results for the IDT are coherent with regard to the IDT of the corresponding counterflow diffusion flames. Additionally, the LES predictions for the concentrations of OH and CH_2O compare well with experimental data. Further, the analysis of the temperature and CH_2O mass-fraction distributions in mixture-fraction space is coherent with experimental observations, which is an indication of the capacity of the numerical methodology to capture the transition from transition from low to high-temperature combustion. With regard to the two reaction mechanisms, the most important difference is that the simulation with the Polimi mechanism predicts shorter ignition delay times than with the Stanford one. Nonetheless the two mechanisms yielded similar predictions for the flame lift-off length and the average temperature on the spray axis.

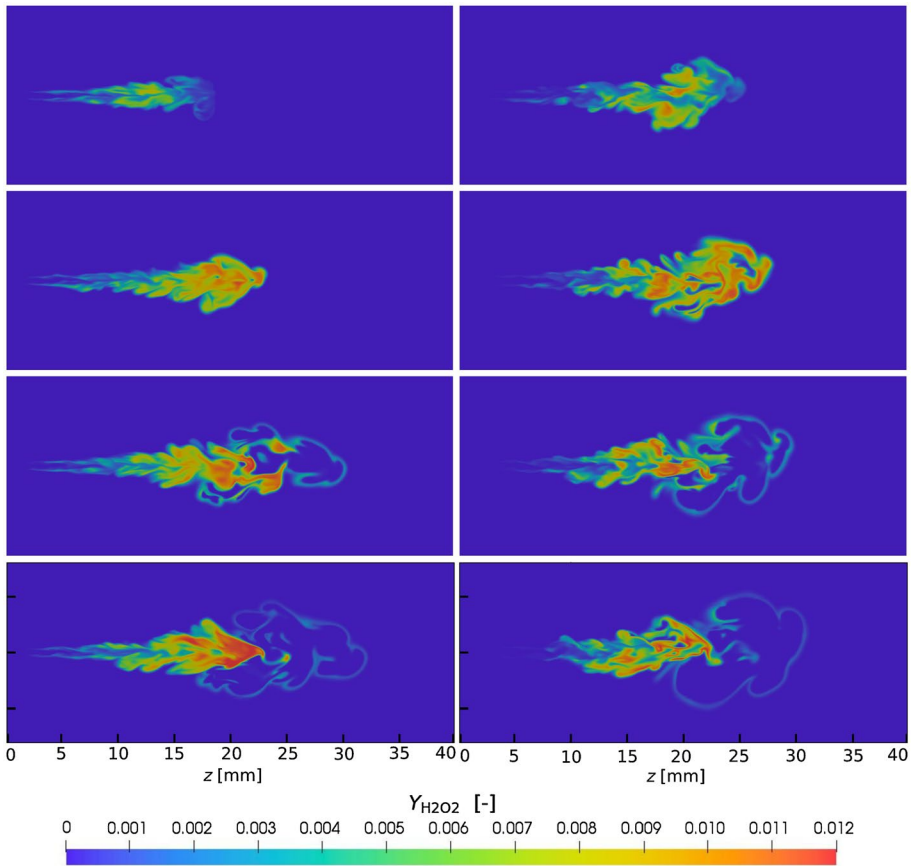


Fig. 13 Color-filled plots of H_2O_2 mass fraction at the central vertical plane and at times shifted relative to the IDT, $t^* = -0.1, -0.05, 0, 0.05$ ms, for the Polimi (left) and the Stanford (center) mechanisms. (For the interpretation of the references to color in this figure legend, the reader is referred to the electronic version of this article.)

Acknowledgements The first author gratefully acknowledges the financial support of the National Research Fund of Belgium (FNRS) in the form of the ERANET BioCFD program.

Funding This study was funded by FNRS (Grant No. R.50.04.17.F).

Availability of data and material All data are available upon request.

Declarations

Conflict of interest The authors declare that they have no conflict of interest.

References

Amsden, A.A., O'Rourke, P.J., Butler, T.D.: KIVA-II: A computer program for chemically reactive flows with sprays. Los Alamos National Lab. REP. LA-11560-MS DE89012805 (1989)

- Balarac, G., Pitsch, H., Raman, V.: Development of a dynamic model for the subfilter scalar variance using the concept of optimal estimators. *Phys. Fluid* **20**, 035114 (2008)
- Barths, H., Hasse, C., Peters, N.: Computational fluid dynamics modelling of non-premixed combustion in direct injection diesel engines. *Int J Engine Res* **1**, 249–267 (2000)
- Bilger, R.W., Stårner, S.H., Kee, R.J.: On reduced mechanisms for methane-air combustion in nonpremixed flames. *Combust Flame* **80**, 135–149 (1990)
- Blombert, C.K., Zeugin, L., Pandurangi, S.S., Bolla, M., Boulouchos, K.: Modeling split injections of ECN Spray A using a conditional moment closure combustion model with RANS and LES. *SAE Int J Eng* **9**, 2107–2119 (2016)
- Borghini, R.: Turbulent combustion modelling. *Progr Energy Combust Sci* **4**, 245–292 (1988)
- Bray, K.N.C., Champion, M., Libby, P.A.: The interaction between turbulence and chemistry in premixed turbulent flames. In: *Turbulent Reactive Flows*, pp. 541–563. Springer, New York, NY (1989)
- Burcat, A., Ruscic, B.: Third millennium ideal gas and condensed phase thermochemical database for combustion (with update from active thermochemical tables). Argonne national laboratory technical report ANL-05/20 and Technion – Israel Inst. of Tech. Report TAE 960 (2005)
- Cernansky, N.P., Friend, D.G., Farrell, J.T., Dryer, F.L., Law, C.K., Pitsch, H., Hergart, C.A., McDavid, R.M., Patel, A.K., Mueller, C.J.: Development of an experimental database and kinetic models for surrogate diesel fuels. In: *SAE World Congress & Exhibition*, pp. 0148–7191. SAE International, Warrendale, PA (2007)
- Chai, X., Mahesh, K.: Dynamic k-equation model for large-eddy simulation of compressible flows. *J. Fluid Mech.* **699**, 385–413 (2012)
- Davidovic, M., Falkenstein, T., Bode, M., Cai, L., Kang, S., Hinrichs, J., Pitsch, H.: LES of n-dodecane spray combustion using a multiple representative interactive flamelets model. *Oil Gas Sci. Technol. - Rev. IFP Energies nouvelles* **72**, 29 (2017)
- Dukowicz, J.K.: A particle-fluid numerical model for liquid sprays. *J. Computat. Phys.* **35**, 229–252 (1980)
- Engine combustion network: Spray A operating condition, (2021). <https://ecn.sandia.gov/diesel-spray-combustion/target-condition/spray-ab/>
- Favre, A.: Turbulence - space-time statistical properties and behavior in supersonic flows. *Phys. Fluid.* **26**, 2851–2863 (1983)
- Ferziger, J., Perić, M., Street, R.: *Computational methods for fluid dynamics*, 4th edn. Springer, Switzerland (2020)
- Fooladgar, E., Chan, C.K., Nogenmyr, K.-J.: An accelerated computation of combustion with finite-rate chemistry using LES and an open source library for In-Situ-Adaptive Tabulation. *Comput. & Fluid.* **146**, 42–50 (2017)
- Goodwin, D.G., Speth, R.L., Moffat, H.K., Weber, B.W.: Cantera: an object-oriented software toolkit for chemical kinetics, thermodynamics, and transport processes. <https://www.cantera.org>. Version 2.5.1 (2021)
- Gribi, B., Lin, Y., Hui, X., Zhang, C., Sung, C.-J.: Effects of hydrogen peroxide addition on combustion characteristics of n-decane/air mixtures. *Fuel* **223**, 324–333 (2018)
- Grosshans, H., Griesing, M., Mönckedieck, M., Hellwig, T., Walther, B., R. Gopireddy, S., Sedelmayer, R., Pauer, W., Moritz, H.U., A. Urbanetz, N., Gutheil, E.: Numerical and experimental study of the drying of bi-component droplets under various drying conditions. *Int. J. Heat Mass Transf.* **96**, 97–109 (2016)
- Grosshans, H., Berrocal, E., Kristensson, E., Szász, R.: Prediction and measurement of the local extinction coefficient in sprays for 3D simulation/experiment data comparison. *Int. J. Multiphase Flow* **72**, 218–232 (2015)
- Issa, R.I.: Solution of the implicitly discretised fluid flow equations by operator-splitting. *J. Computat. Phys.* **62**(1), 40–65 (1986)
- Jurić, F., Stipiš, M., Samec, N., Hriberšek, M., Honus, S., Vujanović, M.: Numerical investigation of multiphase reactive processes using flamelet generated manifold approach and extended coherent flame combustion model. *Energy Convers. Manage.* **240**, 114261 (2021)
- Kahila, H., Wehrfritz, A., Kaario, O., Ghaderi Masouleh, M., Maes, N., Somers, B., Vuorinen, V.: Large-eddy simulation on the influence of injection pressure in reacting spray A. *Combust. Flame* **191**, 142–159 (2018)
- Kee, R.J., Coltrin, M.E., Glarborg, P.: *Chemically reacting flow: theory and practice*, 2st. Wiley, New York, NY (2018)
- Klein, R., Schoen, L.J.: 6. Role of formaldehyde in combustion, pp. 58–68. American Chemical Society, Washington DC (1958)
- Knudsen, E., Kim, S.H., Pitsch, H.: An analysis of premixed flamelet models for large eddy simulation of turbulent combustion. *Phys Fluids* **22**, 1152109 (2010)

- Lessani, B., Papalexandris, M.V.: Time accurate calculation of variable density flows with strong temperature gradients and combustion. *J. Comput. Phys.* **212**, 218–246 (2006)
- Li, S., Wei, X.: Ignition delay characteristics of kerosene with decomposed hydrogen peroxide. *J. Propul. Power* **32**, 431–438 (2016)
- Lillo, P.M., Pickett, L.M., Persson, H., Andersson, O., Kook, S.: Diesel spray ignition detection and spatial/temporal correction. *SAE Int J Engin* **5**, 1330–1346 (2012)
- Liu, A.B., Mather, D., Reitz, R.D.: Modeling the effects of drop drag and breakup on fuel sprays. In: International Congress & Exposition. SAE International, Warrendale, PA (1993)
- Long, A., Speth, R., Green, W.: Ember: an open-source, transient solver for 1d reacting flow using large kinetic models, applied to strained extinction. *Combust Flame* **195**, 1–12 (2018)
- Ma, L., Roekaerts, D.: Modeling of spray jet flame under MILD condition with non-adiabatic FGM and a new conditional droplet injection model. *Combust Flame* **165**, 402–423 (2016)
- Ma, L., Roekaerts, D.: Structure of spray in hot-diluted coflow flames under different coflow conditions: A numerical study. *Combust Flame* **172**, 20–37 (2016)
- Maas, U., Pope, S.B.: Simplifying chemical kinetics: intrinsic low-dimensional manifolds in composition space. *Combust Flame* **3**, 239–264 (1992)
- Maes, N., Meijer, M., Dam, N., Somers, B., Toda, H.B., Bruneaux, G., Skeen, S.A., Pickett, L.M., Manin, J.: Characterization of spray a flame structure for parametric variations in ECN constant-volume vessels using chemiluminescence and laser-induced fluorescence. *Combust Flame* **174**, 138–151 (2016)
- Maghbouli, A., Akkurt, B., Lucchini, T., D'Errico, G., Deen, N.G., Somers, B.: Modelling compression ignition engines by incorporation of the flamelet generated manifolds combustion closure. *Combust Theory Modell* **23**, 414–438 (2019)
- Meyers, R.E., O'Brien, E.E.: The joint pdf of a scalar and its gradient at a point in a turbulent fluid. *Combust Sci Tech* **26**, 123–134 (1981)
- Moin, P., Squires, K., Cabot, W., Lee, S.: A dynamic subgrid-scale model for compressible turbulence and scalar transport. *Phys. Fluid. A: Fluid Dyn.* **3**(11), 2746–2757 (1991)
- Narayananwamy, K., Pepiot, P., Pitsch, H.: A chemical mechanism for low to high temperature oxidation of n-dodecane as a component of transportation fuel surrogates. *Combust Flame* **161**, 866–884 (2014)
- Nguyen, K.-B., Dan, T., Asano, I.: Combustion, performance and emission characteristics of direct injection diesel engine fueled by jatropha hydrogen peroxide emulsion. *Energy* **74**, 301–308 (2014)
- Nicholson, L., Fang, X., Camm, J., Davy, M., Richardson, D.: Comparison of transient Diesel spray break-up between two computational fluid dynamics codes. In: WCX World Congress Experience, pp. 01–0307. SAE International, Warrendale, PA (2018)
- Oldenhof, E., Tummers, M., Veen, E., Roekaerts, D.J.E.M.: Ignition kernel formation and lift-off behaviour of jet-in-hot-coflow flames. *Combust Flame* **157**, 1553–1563 (2010)
- Papalexandris, M.V.: Combustion and fuels. Presses Universitaires Louvain, Belgium (2020)
- Payri, F., García-Oliver, J.M., Novella, R., Pérez-Sánchez, E.J.: Influence of the n-dodecane chemical mechanism on the CFD modelling of the diesel-like ECN spray A flame structure at different ambient conditions. *Combust Flame* **208**, 198–218 (2019)
- Peters, N.: Laminar flamelet concepts in turbulent combustion. Symposium (International) on Combustion **21**, 1231–1250 (1988)
- Peters, N.: Laminar diffusion flamelet models in non-premixed turbulent combustion. *Progr Energy Combust Sci* **10**, 319–339 (1984)
- Pierce, C.D., Moin, P.: A dynamic model for subgrid-scale variance and dissipation rate of a conserved scalar. *Phys Fluid* **10**, 3041–3044 (1998)
- Pierce, D.C., Moin, P.: Progress-variable approach for large-eddy simulation of non-premixed turbulent combustion. *J Fluid Mech* **504**, 73–97 (2004)
- Poinsot, T., Veynante, D.: Theoretical and numerical combustion, 2nd edn. R.T. Edwards Inc., Philadelphia, PA (2005)
- Ranz, W.E., Marshall, W.R.: Evaporation from drops: Part I. *Chem. Engr. Prog.* **48**(3), 141–146 (1952)
- Ranz, W.E., Marshall, W.R.: Evaporation from drops: Part II. *Chem. Engr. Prog.* **48**(3), 173–180 (1952)
- Ranzi, E., Frassoldati, A., Grana, R., Cuoci, A., Faravelli, T., Kelley, A.P., Law, C.K.: Hierarchical and comparative kinetic modeling of laminar flame speeds of hydrocarbon and oxygenated fuels. *Progress in energy and combustion science* **38**, 468–501 (2012)
- Ranzi, E., Frassoldati, A., Stagni, A., Pelucchi, M., Cuoci, A., Faravelli, T.: Reduced kinetic schemes of complex reaction systems: Fossil and biomass-derived transportation fuels. *Int J Chem Kinet* **46**, 512–542 (2014)
- Ribert, G., Champion, M., Gicquel, O., Darabiha, N., Veynante, D.: Modeling nonadiabatic turbulent premixed reactive flows including tabulated chemistry. *Combust Flame* **141**, 271–280 (2005)

- Robin, V., Mura, A., Champion, M., Plion, P.: A multi-dirac presumed PDF model for turbulent reactive flows with variable equivalence ratio. *Combust Science Tech* **178**, 1843–1870 (2006)
- Salehi, F., Cleary, M.J., Masri, A.R., Ge, Y., Klimenko, A.Y.: Sparse-Lagrangian MMC simulations of an n-dodecane jet at engine-relevant conditions. *Proceed Combust Institute* **36**, 3577–3585 (2017)
- Sarathy, S.M., Westbrook, C.K., Mehl, M., Pitz, W.J., Togbe, C., Dagaut, P., Wang, H., Oehlschlaeger, M.A., Niemann, U., Seshadri, K., Veloo, P.S., Ji, C., Egolfopoulos, F.N., Lu, T.: Comprehensive chemical kinetic modeling of the oxidation of 2-methylalkanes from C7 to C20. *Combust Flame* **158**, 2338–2357 (2011)
- Sirignano, W.A.: *Fluid dynamics and transport of droplets and sprays*. Cambridge University Press, UK (2010)
- Skeen, S.A., Manin, J., Pickett, L.M.: Simultaneous formaldehyde PLIF and high-speed schlieren imaging for ignition visualization in high-pressure spray flames. *Proceed Combust Institut* **35**, 3167–3174 (2015)
- Stahl, G., Warnatz, J.: Numerical investigation of time-dependent properties and extinction of strained methane- and propane-air flamelets. *Combust Flame* **85**, 285–299 (1991)
- Sula, C., Grosshans, H., Papalexandris, M.: Assessment of droplet breakup models for spray flow simulations. *Flow, Turbulen Combust* **105**, 889–914 (2020)
- Sutherland, J.C., Smith, P.J., Chen, J.H.: Quantification of differential diffusion in nonpremixed systems. *Combust Theory Modell* **9**, 365–383 (2005)
- Tekgül, B., Kahila, H., Kaario, O., Vuorinen, V.: Large-eddy simulation of dual-fuel spray ignition at different ambient temperatures. *Combust Flame* **215**, 51–65 (2020)
- Van Oijen, J.A., De Goey, L.P.H.: Modelling of premixed laminar flames using flamelet-generated manifolds. *Combust Sci Tech* **161**, 113–13 (2000)
- Vervisch, L., Hauguel, R., Domingo, P., Rullaud, M.: Three facets of turbulent combustion modelling: DNS of premixed V-flame, LES of lifted nonpremixed flame and RANS of jet-flame. *J Turbulence* **5**, 4 (2004)
- Wehrfritz, A.: *Large eddy simulation of fuel spray combustion*. Doctoral Dissertation, Aalto University, Finland (2016)
- Wehrfritz, A., Kaario, O., Vuorinen, V., Somers, B.: Large eddy simulation of n-dodecane spray flames using flamelet generated manifolds. *Combust Flame* **167**, 113–131 (2016)
- Weller, H.G., Tabor, G., Jasak, H., Fureby, C.: A tensorial approach to computational continuum mechanics using object-oriented techniques. *Comput Phys* **12**, 620–631 (1998)
- Wilke, C.: A viscosity equation for gas mixtures. *J Chem Phys* **18**, 517–519 (1950)
- Xue, Q., Som, S., Senecal, P.K., Pomraning, E.: Large eddy simulation of fuel-spray under non-reacting IC engine conditions. *Atomizat Spray* **23**, 925–955 (2013)
- Yoshizawa, A.: Statistical theory for compressible turbulent shear flows, with the application to subgrid modeling. *Phys Fluid* **29**, 2152–2164 (1987)
- Zhang, Y., Xu, S., Zhong, S., Bai, X.-S., Wang, H., Yao, M.: Large eddy simulation of spray combustion using flamelet generated manifolds combined with artificial neural networks. *Energy AI* **2**, 100021 (2020)
- Zhang, Y., Wang, H., Both, A., Ma, L., Yao, M.: Effects of turbulence-chemistry interactions on auto-ignition and flame structure for n-dodecane spray combustion. *Combust Theory Modell* **23**, 907–934 (2019)